Available online at www.sciencedirect.com
ScienceDirect
Geochimica et Cosmochimica Acta 71 (2007) 1967–1981
Geochimica et Cosmochimica Acta
www.elsevier.com/locate/gca

Ba and Ni speciation in a nodule of binary Mn oxide phase composition from Lake Baikal

Alain Manceau [a,*], Michael Kersten [b], Matthew A. Marcus [c], Nicolas Geoffroy [a], Liba Granina [d]

[a] Environmental Geochemistry Group, LGIT, University J. Fourier and CNRS, BP 53, F-38041 Grenoble Cedex 9, France
[b] Geosciences Institute, Johannes Gutenberg-University, D-55099 Mainz, Germany
[c] Advanced Light Source, Lawrence Berkeley National Laboratory, One Cyclotron Road, Berkeley, CA 94720, USA
[d] Limnological Institute, Russian Academy of Science, Irkutsk 664033, Russia

Received 17 October 2006; accepted in revised form 5 February 2007; available online 21 February 2007

Abstract

The partitioning and incorporation mechanism of Ni and Ba in a ferromanganese nodule from Lake Baikal were characterized by X-ray microfluorescence, microdiffraction, and absorption spectroscopy. Fe is speciated as goethite, and Mn as romanechite (psilomelane) and 10 Å-vernadite (turbostratic buserite) with minor 7 Å-vernadite (turbostratic birnessite). Barium is associated with romanechite and Ni with vernadite in distinct and irregularly distributed layers, and each type of Mn oxide is separated from the other type by goethite. The binary Mn oxide banding pattern is interpreted by a two-mode accretionary model, in which the variation in Ba flux induced by hydrothermal water pulses determines whether a tectomanganate (romanechite) or phyllomanganate (vernadite) is formed during the ferromanganese nodule accretion. Consistent with the dependence of Ni sorption on pH and the circumneutral pH of the lake water, nickel is mainly substituted isomorphically for Mn in the manganese layer, and is not sorbed at vacant Mn layer sites in the interlayer.

1. INTRODUCTION

Lake Baikal in southeastern Siberia is one of the oldest lakes in the world, with an age of around 30 million years. The basin of Lake Baikal belongs to a particular class of rift basins that originate from subsidence along major border faults, resulting in the particular long, deep and narrow shape of the lake trench. It is the world's largest body of fresh surface water, with a maximum depth of 1642 m, and belongs to the category of ultra-fresh calcium bicarbonate water of a pH 7.6, with a dissolved salt content below 100 mg L^{-1} (Votintsev, 1961). The concentrations of most elements in the water column are controlled by weathering of surrounding rocks, and the riverine input is consequently the major source comprising 75% to >99% (97% on average). A major feature that sets Lake Baikal apart from other deep lakes is that its entire water column is constantly enriched with oxygen due to its oligotrophic status (low biological productivity results in a small amount of degradable organic matter), and regular deep-water renewal with oxygen-rich surface waters (Votintsev, 1961; Granina et al., 2000). In the water 2–5 mm above the bottom the oxygen content is never less than 230 μmol L^{-1} (Martin et al., 1998). The sediment surface is orange-brown and enriched in Fe and Mn oxyhydroxides, and the oxidized layer is from <1 to 20–30 cm thick, depending on the oxygen penetration depth, and thus on the sedimentation rate (Granina et al., 2000). Another peculiarity of this freshwater system is a subaquatic hydrothermal point source (vent system) located in the region of Frolikha Bay (Northern Baikal). The hydrothermal activity is characterized by increased heat flux from the bottom (Crane et al., 1991; Golubev et al., 1993), excess of crustal ^4He in bottom waters (Kipfer et al., 1996),

* Corresponding author. Fax: +33 4 76 82 81 01.
E-mail addresses: Alain.Manceau@obs.ujf-grenoble.fr, Manceau@ujf-grenoble.fr (A. Manceau).

0016-7037/$ - see front matter © 2007 Elsevier Ltd. All rights reserved.
doi:10.1016/j.gca.2007.02.007

peculiarities in chemistry and stable isotope composition in pore waters at the hydrothermal discharge site (Callender and Granina, 1992; Shanks and Callender, 1992; Granina et al., 2002, 2007), and a specific and rather diverse fauna (Gebruk, 1995). Although such hydrothermal manifestations are frequent in extensional tectonic settings, no other vent sites have been found yet in the Baikal rift lake.

Distinct zones of sedimentary Fe and Mn oxyhydroxides are known to occur within the sediments of Lake Baikal (Leybovich, 1983; Granina, 1992a,b; Granina et al., 2000, 2004; Müller et al., 2002). They spread over all three lakes' basins, and also exist on the underwater Academician Ridge that separates the northern and central basins. In many locations extended layers occur in near-surface sediments, with the top part enriched in Mn and the bottom part in Fe. At some locations, solid Fe/Mn crusts up to 1 cm thick are formed at the oxic–anoxic interface. A low sedimentation rate on the order of 0.01–1 mm yr^{-1}, and a low content of sedimentary organic carbon of about 2 wt.% on average, is a prerequisite for the post-depositional formation and preservation of such layers and crusts (Granina, 1992b; Granina et al., 2000, 2004). The Mn content in the enriched layers ranges from 10^{-5} mol cm^{-3} at sites of higher sedimentation rate near the Selenga Delta, and up to 10^{-2} mol cm^{-3} at the Academician Ridge where the sedimentation rate is the lowest and the elements scavenged are of autochthonous origin (hydrogeneous accretion mode).

The ferromanganese precipitates have a Fe/Mn ratio of ~17 on average in shallow water crusts and concretions, and down to ~1.4 in deep-water crusts (Granina, 1992a; Deike et al., 1997). Globe-shaped Mn-rich ferromanganese nodules have been found on the northern slope of Bolshoi Ushkanii Island in Northern Baikal during a cruise of submarine "Pisces" in 1990. These nodules had Fe/Mn ratios lower than all other ferromanganese precipitates previously known from the lake, and were enriched in Co, Ni, Cu, and especially Ba (Bukharov et al., 1992; Amirzhanov et al., 1993).

Although ferromanganese precipitates have been studied extensively over the past decades, it is only within the last few years that insights have been gained into the speciation of their trace element inventory (Marcus et al., 2004a, and references therein). In this paper, we examine the speciation of Ni and Ba in one of these Northern Baikal nodules using the combination of synchrotron-based X-ray micro-fluorescence (μ-XRF), micro-diffraction (μ-XRD), and micro and powder extended X-ray absorption fine structure (EXAFS) spectroscopy (Manceau et al., 2002a). The first technique was used to map Mn, Fe, Ni, and Ba distributions, and to identify elemental associations. Based on these maps, the nature of the minerals hosting Ni and Ba then was deduced from μ-XRD and Mn-EXAFS spectroscopy. Finally, with Ni- and Ba-EXAFS spectroscopy, the structural relationship between the trace metals and mineral hosts was examined.

2. MATERIALS AND METHODS

2.1. Sample

The ferromanganese nodule sample Pa-1 used for this study was described in detail earlier together with another sample Pa-2 of similar composition (Bukharov et al., 1992; Amirzhanov et al., 1993; Bukharov and Fialkov, 1996). Both samples were collected from the northern slope of the Bolshoi Ushkanyi Island at 510 m depth (Electronic Annex EA-1). The originally subspherical sample Pa-1 of about 2 cm in diameter was encased in epoxy resin and cut in half along its longest axis to obtain cross sections in a plane that included the direction of its highest accretion rate. A thin section of one of the cut surfaces revealed in reflected light a strong texture characterized by zones of botryoidal layering, with individual layers having thicknesses from tens to hundreds of microns. Semi-quantitative electron probe microanalysis (Electronic Annexes EA-2 and EA-3) showed large variations in chemical composition, with about 8–54% MnO, 7–57% Fe_2O_3, and up to 6.6% BaO and 1.4% NiO. A self-supporting 30-μm thick micropolished section was prepared for synchrotron radiation-based X-ray analysis.

2.2. X-ray measurements

Micro-XRF, μ-XRD, and μ-EXAFS measurements were performed on beamline 10.3.2 at the Advanced Light Source (ALS), Berkeley. The beam spot of the microspectrometer can be adjusted from 16 (H) × 7 (V) to 5 × 5 μm^2 (Manceau et al., 2002a; Marcus et al., 2004b). The distributions of Mn, Fe, Ni and Ba were imaged by scanning the sample under a monochromatic beam and measuring the intensity of the Kα (Mn and Ni), Kβ (Fe) and Lα (Ba) fluorescence lines with a 7-element Ge solid-state detector and a counting time of 100–150 ms per pixel. The intensities of the Kα and Kβ radiation were recorded with an excitation energy of 10 keV, and that of the Ba(Lα) radiation by subtracting the Ti(Kα) intensity measured at 5197 eV (Ba L_3 −50 eV) from the Ba(Lα) + Ti(Kα) intensity at 5297 eV (Ba L_3 +50 eV). The fluorescence yield was normalized against the incident intensity I_0 and the counting time. No attempt was made to calculate elemental concentrations because of the difficulties inherent to this type of quantification, and the focus was on relative element distributions, mineralogy and crystal chemistry of the sample. Elemental distributions were portrayed with a RGB (red, green, blue) color scheme, by assigning two (bicolor map) or three (tricolor map) primary colors to different elements (Manceau et al., 2002a). When fluorescence signals from these elements overlap, the primary colors mix in proportion to the fluorescence intensities and produce a secondary color: green + blue = cyan, green + red = yellow, blue + red = magenta, and red + green + blue = white. The μ-XRD patterns were recorded in transmission with a Bruker 6000 CCD binned to 1024 × 1024 pixels at 14 keV incident X-ray energy and 16 × 7 μm beam size. The two-dimensional XRD patterns were calibrated with corundum (α-Al_2O_3) and integrated to one-dimensional patterns with the Fit2d code (Hammersley et al., 1996). Mn K-edge, Ni K-edge, and Ba L_3-edge μ-EXAFS spectra were collected at different spots on the sample, representing either Ba- or Ni-rich regions. To avoid possible radiation damage, only one spectrum was collected at each spot, and spectra from nearby (~10 μm spacing) spots having similar compositions and

mineralogy, as seen from the XRF maps and μ-XRD patterns, were averaged. Several single-scan Ba and Ni spectra were recorded at distant spots throughout the thin section to verify the uniqueness of Ba and Ni speciation. Also, a wide-beam (300 × 150 μm) Ni-EXAFS spectrum was collected on beamline FAME (Proux et al., 2006) at the European synchrotron radiation facility (ESRF, Grenoble, France) on a sample powder. All Ba-EXAFS spectra were statistically indistinguishable, showing that the Ba speciation was unique. The Ni-EXAFS spectra, although distinct from those for Ba, also indicated a single Ni species by their lack of statistically significant variation. EXAFS data were analyzed by standard procedures (Teo, 1986).

3. RESULTS

3.1. XRF maps

The alternating Fe-rich (green) and Mn-rich (blue) bands are depicted in the bicolor map of Fig. 1a. When Ba is added in red, the Mn layers from the lower right region are magenta, some in the middle and upper left region are dark violet, and others from the middle region remain blue (Fig. 1b). In contrast, these blue layers become magenta when Ni is imaged in red (Fig. 1c). Thus, Ba and Ni are associated with Mn, and mostly anti-correlated. A Ba association with Mn rather than with Fe is common in ferromanganese precipitates (Manceau et al., 2007), and was reported in samples from Lake Tomahawk (USA) and Lake Biwa (Japan) (Jones and Bowser, 1978; Sugiyama et al., 1992). The negative relationship between Ba and Ni is imaged in Fig. 1d with Ba in blue and Ni in red. This map contains blue and red layers, but also some magenta and dark violet layers, suggesting an incomplete separation of Ba and Ni. Mineralogical and spectroscopic data presented below show that these two elements are associated with two distinct Mn oxides, which are completely separated in the monochromatic layers and mixed in the bicolored layers from Fig. 1d.

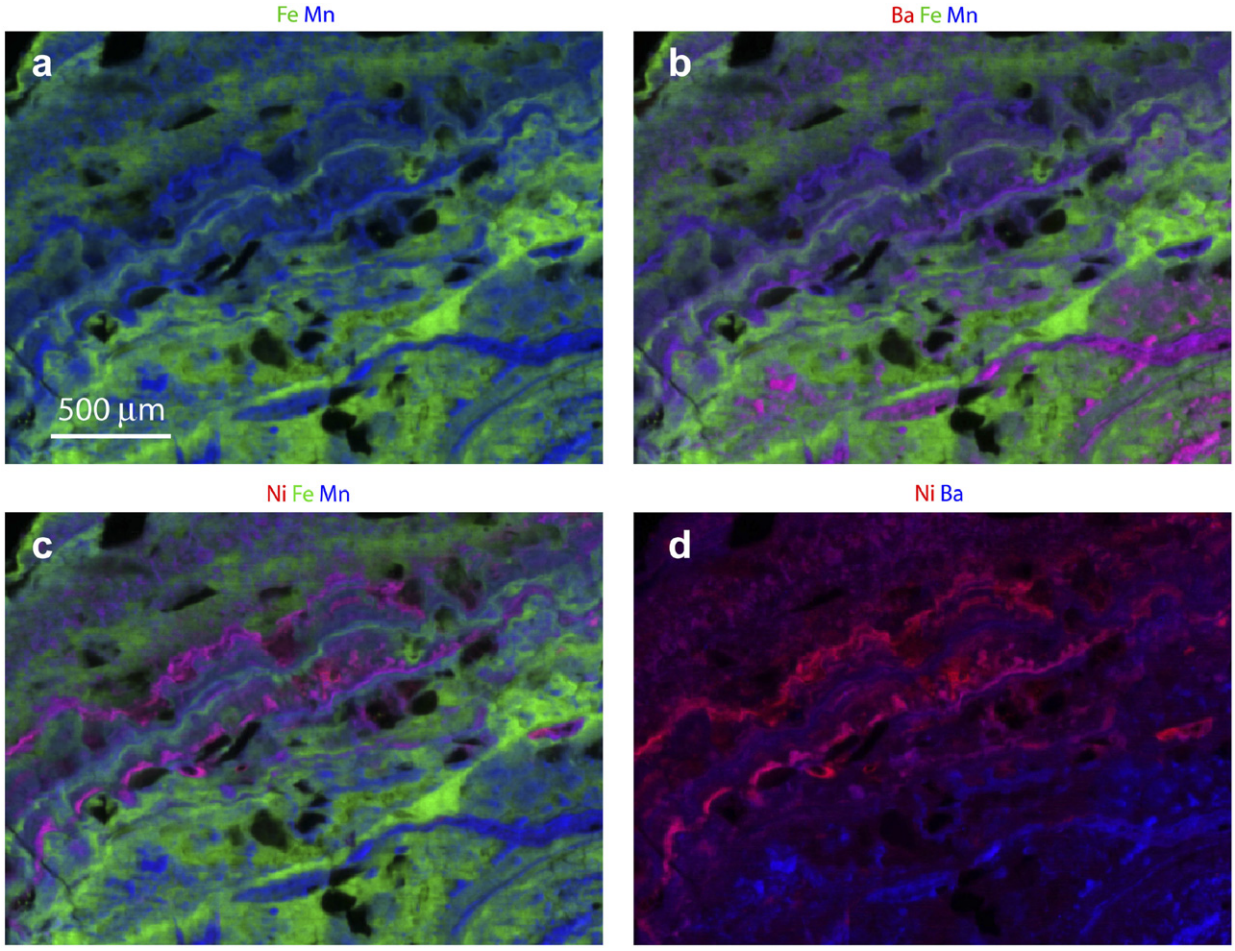

Fig. 1. Micro-XRF fine map of the distribution of Mn, Fe, Ba, and Ni in a ferromanganese nodule from Lake Baikal. The color coding is: (a) green = Fe, blue = Mn; (b) red = Ba, green = Fe, blue = Mn; (c) red = Ni, green = Fe, blue = Mn; (d) red = Ni, blue = Ba. Each pixel is colored in proportion to the normalized fluorescence signals. Size = 2500 (H) × 1800 (V) μm^2, pixel resolution and beam size = 5 × 5 μm^2, counting time = 150 ms/pixel.

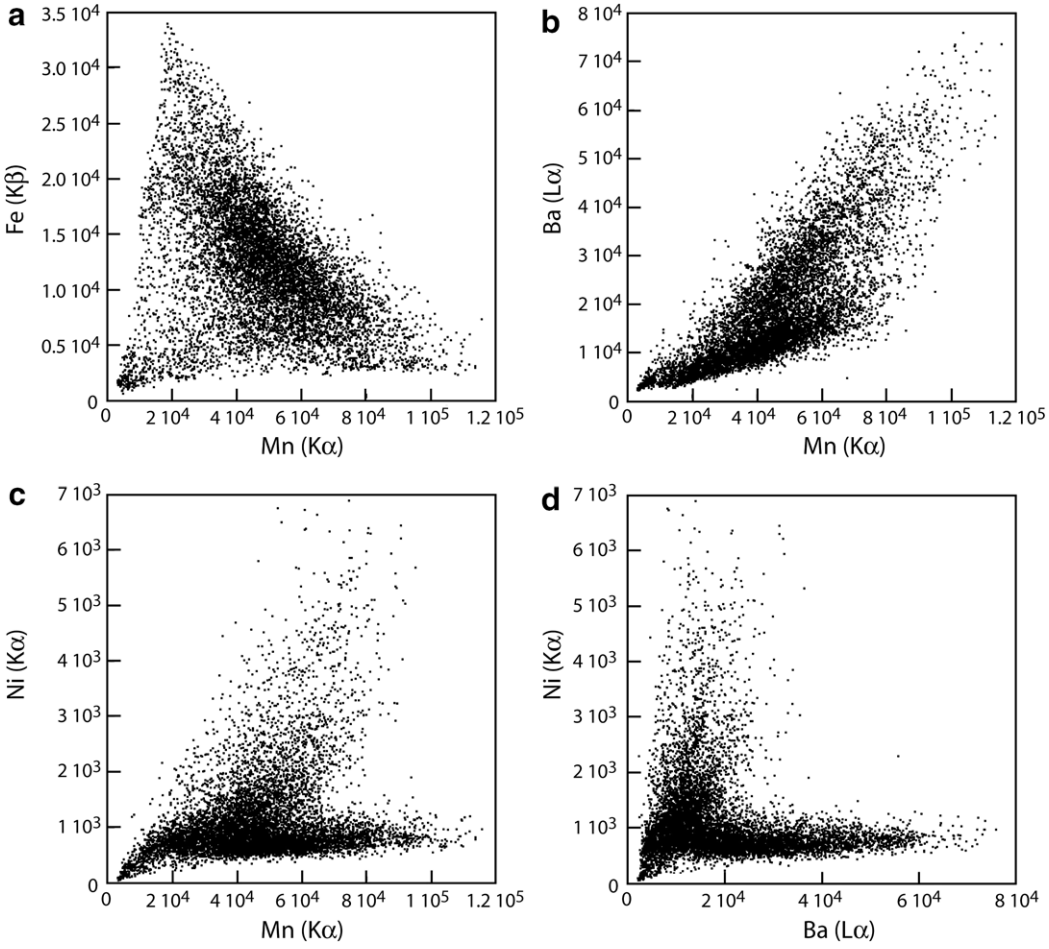

Fig. 2. Scatter plots of the normalized fluorescence counts between Fe and Mn (a), Ba and Mn (b), Ni and Mn (c), and Ni and Ba (d).

Elemental correlations were evaluated in more detail by representing the fluorescence intensities from the previous maps as scatter plots (Fig. 2; Manceau et al., 2002a). The Fe vs. Mn plot reveals that the scanned region contains areas in which the two major elements are well separated, and others which are permeated with both Fe and Mn. The average Fe/Mn ratio is about 1, as estimated from the relative intensities of the Fe(Kβ) and Mn(Kα) signals, correcting the data for air absorption, fluorescence yields, and taking I[Fe(Kα)]/I[Fe(Kβ)] = 100/17. Chemically, the most differentiated bands contain about 5–10 times more of one major element over the other. The Ba–Mn and Ni–Mn populations are distinguished in the scatter plots of Fig. 2b and c by rays of differing slopes. The Ni–Ba plot shows mainly two rays along the axes, confirming that where Ba is concentrated, Ni is not, and vice versa. The Ba–Mn scatterplot has a Pearson correlation $r = 0.95$, and the Ni–Mn scatterplot $r = 0.74$. The variability of the Ba/Mn and Ni/Mn ratios explains the non-uniformity of the magenta hue in Fig. 2b and c. Close examination of the two maps shows that the variations in hue are more pronounced for Ni than for Ba in this region of the sample, in agreement with the lower r value of the Ni–Mn population. Two other regions of the same ferromanganese nodule were mapped, a large 4880×3000 μm^2 area at 20×20 μm^2 resolution, and a 3400×2300 μm^2 area at 10×10 μm^2 resolution. Results are similar to those presented in this section (Electronic Annex EA-4).

Fig. 3. Powder microdiffraction patterns taken at a Ba-rich spot (a) and two Ni-rich spots (f,g), and powder diffraction patterns from references. (b) Romanechite standard from Hufgard quarry, Germany, (c) todorokite standard from Todoroki mine, Japan, (d) hydrothermal ferromanganese oxide from the Costa Rica margin (Bodei et al., 2006), (e) diagenetic marine ferromanganese oxide from Takahashi et al. (2007) (sample coded as 'D465 outer' in this article). 6KR is a natural vernadite (Manceau et al., 2007). Peaks labeled with an asterisk are from todorokite. 1W and 2W denote one- and two-water layer hydrates, respectively. The wavevector q is defined as $2\pi/d$, with d the d-spacing. The d-values of vernadite were calibrated using the X-ray lines of quartz. Theoretical values for quartz are in parenthesis. The accuracy is better that 0.01 Å over the whole q-range. The two hk bands at 2.45–2.46 Å and 1.41–1.42 Å are indexed by choosing a C-centered layer cell (Villalobos et al., 2006).

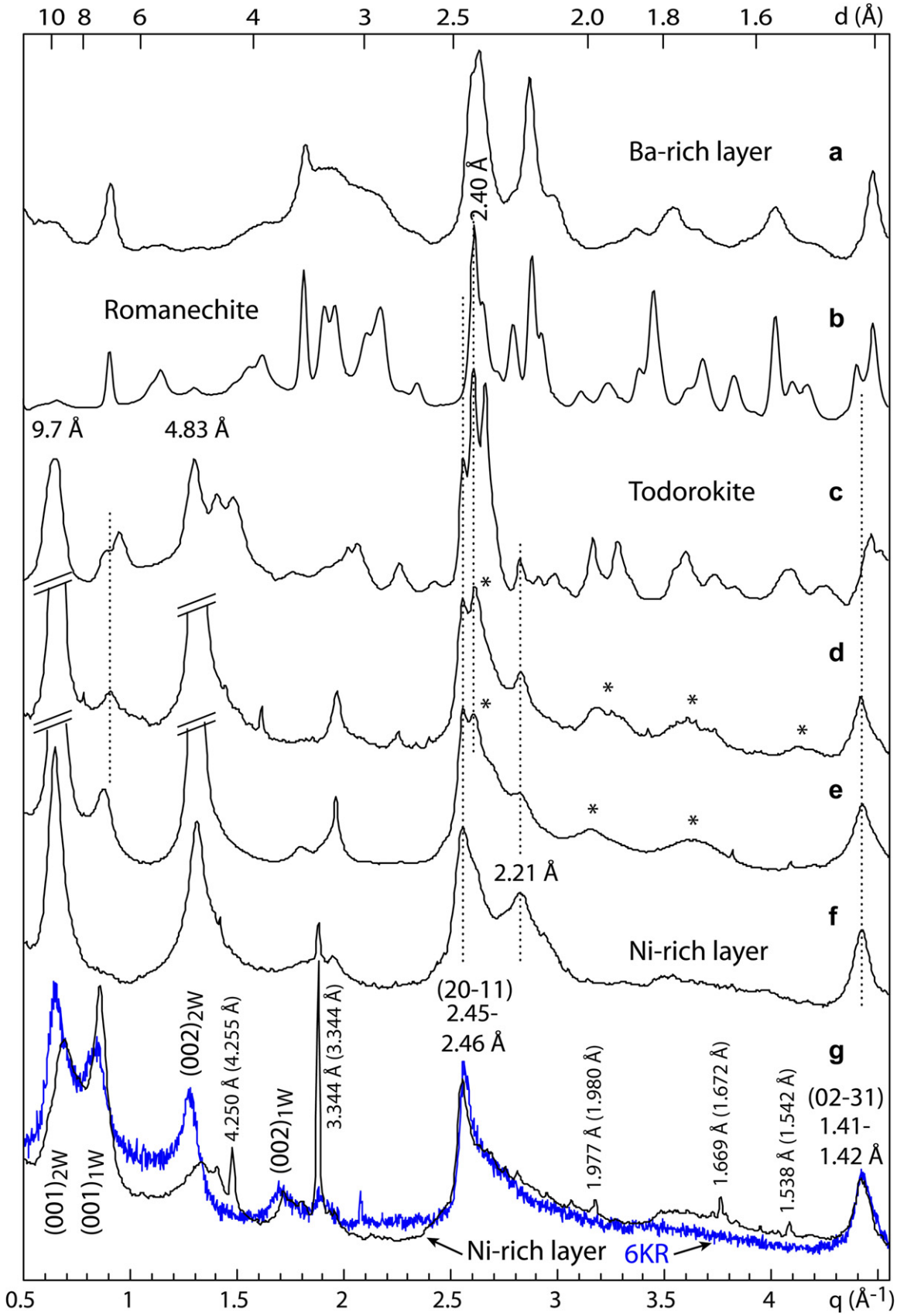
10 8 6 4 3 2.5 2.0 1.8 1.6 d (Å)
Ba-rich layer
a
2.40 Å
Romanechite
b
9.7 Å
4.83 Å
Todorokite
c
d
e
2.21 Å
f
Ni-rich layer
(20-11)
2.45-
2.46 Å
(002)2W
4.250 Å (4.255 Å)
(002)1W
3.344 Å (3.344 Å)
1.977 Å (1.980 Å)
1.669 Å (1.672 Å)
1.538 Å (1.542 Å)
g
(02-31)
1.41-
1.42 Å
(001)2W
(001)1W
Ni-rich layer
6KR
0.5 1 1.5 2 2.5 3 3.5 4 q (Å-1)

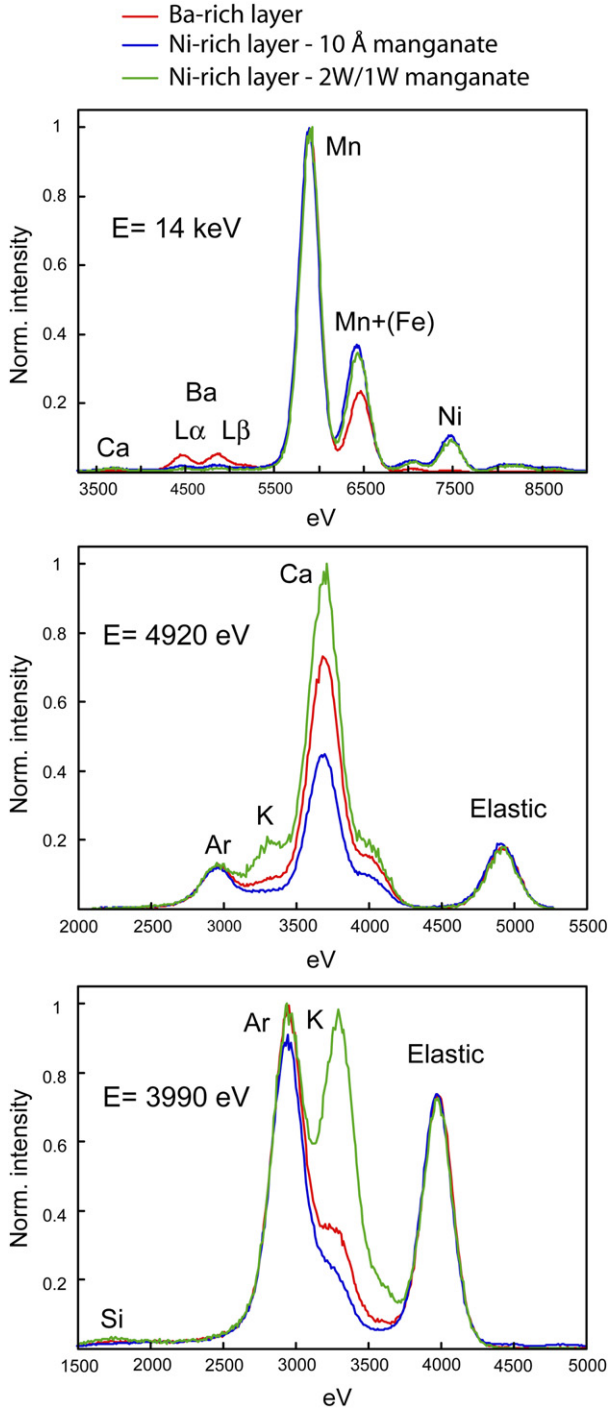

Fig. 4. Characteristic micro-fluorescence spectra of the Ba-rich species and the two Ni-rich species (10 Å and 2W/1W manganates) taken at $E = 14$ keV (top graph), 4920 eV (i.e., below the Ti K-edge; middle graph), and 3990 eV (i.e., below the Ca K-edge; bottom graph).

3.2. X-ray microdiffraction

Two-dimensional μ-XRD patterns were collected on 20 spots rich in Fe, Ni, or Ba. All patterns contained continuous rings of constant intensity along the ring perimeters. Since the X-ray beam had a micrometer size, these powder rings arise from nanometer-sized particles (Manceau et al., 2002a; Electronic Annex EA-5). The diffraction rings from the Fe layers and Fe-rich matrix between the Mn layers matched the *d*-spacings for goethite. No other Fe oxide was detected. Some patterns also contained spotty reflections from coarse grains of quartz, feldspar, or mica. The nature of the Mn phases was identified from the radially integrated and background-subtracted one-dimensional patterns (Fig. 3) and the X-ray fluorescence spectra recorded at the same spots as the 2D patterns (Fig. 4).

All patterns from the Ba-rich, Ni-poor layers were similar and, except for the 1.77 Å reflection ($q = 3.54$ Å^{-1}), had rings matching the position of the most prominent powder diffraction lines of romanechite (or psilomelane), a tectomanganate with 3×2 tunnel structure (Wadsley, 1953; Turner and Buseck, 1979; Turner and Post, 1988) (Fig. 3a and b). The romanechite specimen from Lake Baikal has smaller crystallites than the reference, as indicated by the broadness of its diffraction peaks. All patterns in Ni-rich, Ba-poor layers look like the one shown in Fig. 3f, with one exception shown in Fig. 3g. The most common patterns have basal diffraction maxima at 9.7 Å (001 reflection) and 4.8 Å (002 reflection), and *hk* bands at 2.455 ± 0.005 Å (20−11 reflection) and 1.415 ± 0.005 Å (02−31 reflection) that match known diffraction features of 10 Å-vernadite, also named buserite (a discussion on the nomenclature of disordered phyllomanganates can be found in Manceau et al., 2007) (Giovanoli et al., 1970, 1975; Giovanoli and Bürki, 1975; Usui and Mita, 1995). The high intensity of the two basal reflection indicates that vernadite nanoparticles are not intermixed or intergrown with Fe oxide nanoparticles (e.g. ferrihydrite) at the nanoscale, as observed in so-called Fe-vernadite (Burns and Burns, 1979; Manceau and Combes, 1988; Varentsov et al., 1991; Manceau et al., 1992, 2007; Vodyanitskii et al., 2003, 2004). The *d*-spacings of the 20−11 and 02−31 reflections are in the ratio of $\sqrt{3}$, which indicates that the phyllomanganate layers have hexagonal symmetry with unit cell parameters $a = b \sim 2.83$ Å (Drits et al., 1997). The low value of the layer-cell dimension is an indication that the layers do not contain detectable Mn^{3+} (Manceau et al., 1997; Gaillot et al., 2007), in agreement with the oxidizing sample environment. As a comparison, synthetic hexagonal birnessite (HBi) equilibrated at pH 4 has 13% Mn^{3+} in its layer and *a* and *b* parameters of 2.848 Å (Lanson et al., 2000). Also, lithiophorite $(Al_{0.67}Li_{0.32})(Mn^{4+}_{0.68}\ Mn^{3+}_{0.32})O_2(OH)_2$, which contains 32% of layer Mn^{3+} (Yang and Wang, 2003; Manceau et al., 2005), has $a = b = 2.925$ Å (Post and Appleman, 1994). The scattering tail of the high-*q* asymmetrical 20−11 reflection is modulated by a broad reflection at 2.20–2.22 Å. This reflection could not be assigned to any coexisting mineral species and, thus, is part of the phyllomanganate pattern. This reflection has never been observed on synthetic vernadite (δ-MnO_2), and its structural origin in natural samples has been discussed by Varentsov et al. (1991).

The asymmetrical shape of the 20−11 reflection towards higher *q* values is strong evidence that the 10 Å-manganate has a layer structure. Here a parallel can be made with smectites, whose 02–11 band is also asymmetrical on the right side due to the lack of 3D periodicity (Brindley and Brown, 1980; Drits and Tchoubar, 1990). The reflec-

tions near 10 and 2.4–2.3 Å cannot be attributed to todorokite, a tectomanganate with 3×3 tunnel structure (Post et al., 2003), because this interpretation is inconsistent with the positions and relative intensities of other reflections. The possibility of a phyllomanganate–todorokite mixture also can be dismissed from the comparison with marine samples containing the two phases (Figs. 3d and e). Todorokite has a prominent diffraction line at 2.40 Å, seen as a second maximum to the right of the 20−11 reflection for the phyllomanganate, when the two phases are mixed. Also, the admixture of todorokite modulates the pattern of vernadite between the 20−11 and 02−31 reflections because todorokite has three intense lines in this region, and the phyllomanganate pattern has none.

The distinct phyllomanganate pattern recorded at one Ni-rich spot out of ten analyzed by μ-XRD has no reflection at 2.20–2.22 Å, and exhibits two sets of 001 and 002 basal reflections, one at 9.1 and 4.7 Å, and another at 7.3 and 3.6 Å, from two-water (2W) layer and one-water (1W) layer diffracting crystallites, respectively. This pattern is extremely similar to that described recently for a vernadite specimen (6KR) formed naturally at the surface of quartz grains from sand filters used in groundwater treatment plants (Manceau et al., 2007). The overlay plot of the two vernadite patterns shows that the two samples do not have the same proportions of 1W and 2W crystallites. Revealing information regarding the average layer composition of each diffracting unit is deduced from the following observations. First, in the new sample the 001 reflection of the 2W component is more asymmetrical and further shifted in the direction of the 1W component than in the quartz coating. Second, the 001 reflection of the 2W component is broader than that of the 1W component. Third, the two basal reflections are irrational for the 2W component (9.1 and 4.7 Å), and rational for the 1W component (7.3 and 3.6 Å). In contrast, the 2W basal reflections have less irrationality (9.7 and 4.9 Å) in the quartz coating.

All these observations, put together, indicate that the 2W crystallites consist of a random interstratification of 2W and 1W layers, while the 1W crystallites contain only, or predominantly, 1W layers (Reynolds, 1989; Manceau et al., 2007). In mixed-layer compounds, the exact position of $d(001)$ depends on the relative proportions of the two types of layers (Reynolds, 1989). Since the 001 reflection of the 2W component is closer to 9.7 Å than 7.3 Å, the fraction of the 2W layer hydrates is higher than 50%. However, not all 2W diffracting units contain the same proportion of 1W layers, as indicated by the tail of the 001 peak towards smaller d spacings (i.e., higher q values). Microfluorescence analysis of 2W–1W vernadite revealed that its interlayer contains K and Ca, whereas only Ca was detected at all other Mn spots

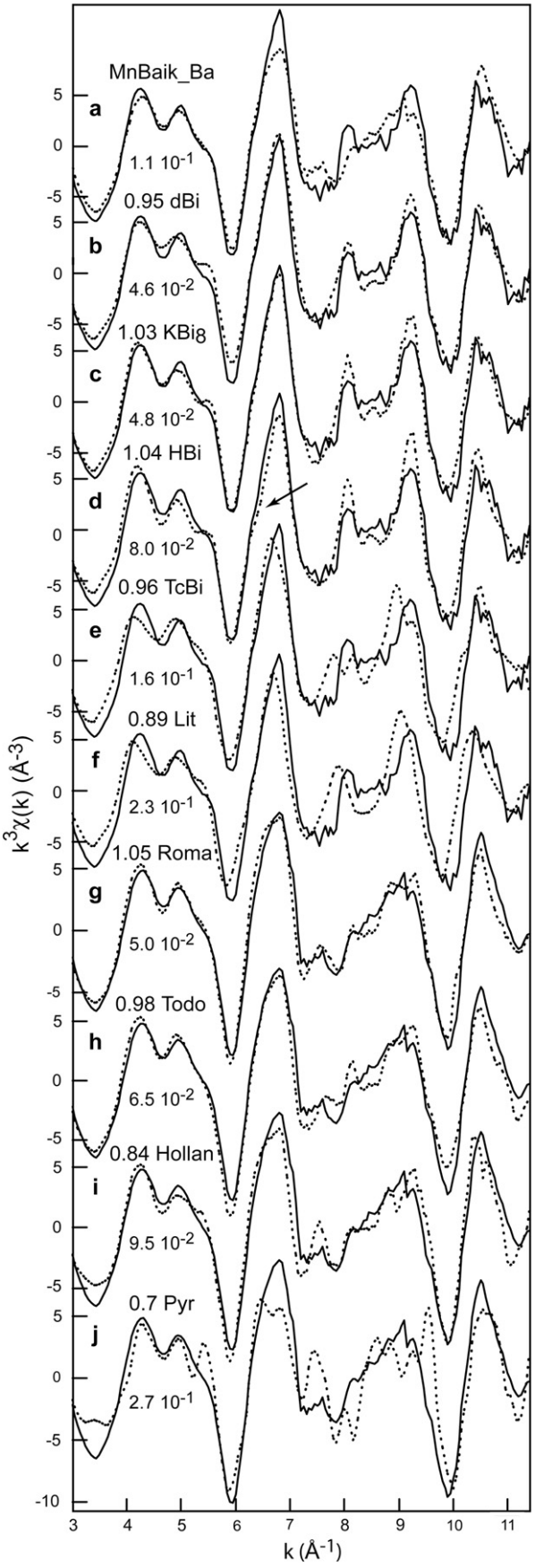

Fig. 5. (a) Micro Mn-EXAFS spectra taken at a Ni-rich spot (MnBaik_Ni, solid line) and at a Ba-rich spot (MnBaik_Ba, dotted line). (b–f) Comparison of the MnBaik_Ni spectrum (solid line) with references (dotted lines). (g–j) Comparison of the MnBaik_Ba spectrum (solid line) with references (dotted lines). The value attached to each plot is the squares of the residuals, normalized to the sum of the squares of the data values (Norm. Sum-Sq), calculated over the [3.0–11.4 $Å^{-1}$] k interval.

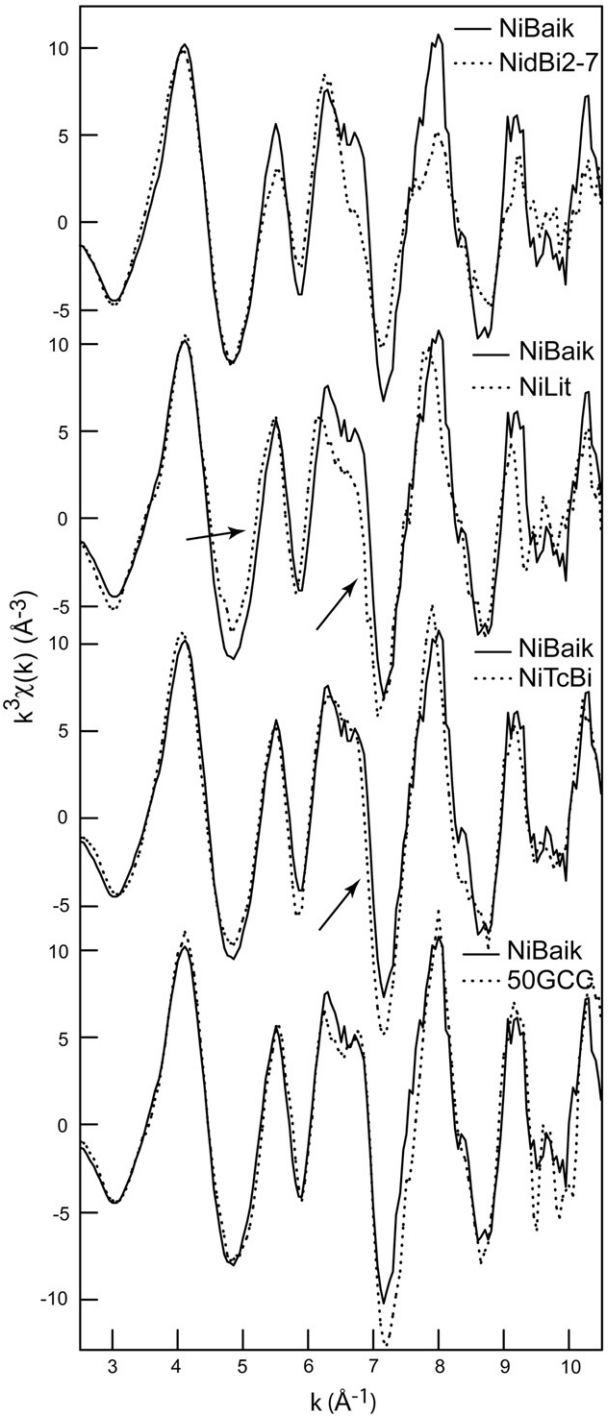

Fig. 6. Ni K-edge EXAFS spectrum of the sample (NiBaik, solid line) and references (dotted lines). Arrows point out the frequency differences which occur when the Mn layer has Mn^{3+} (i.e., Ni–Mn^{3+} pairs).

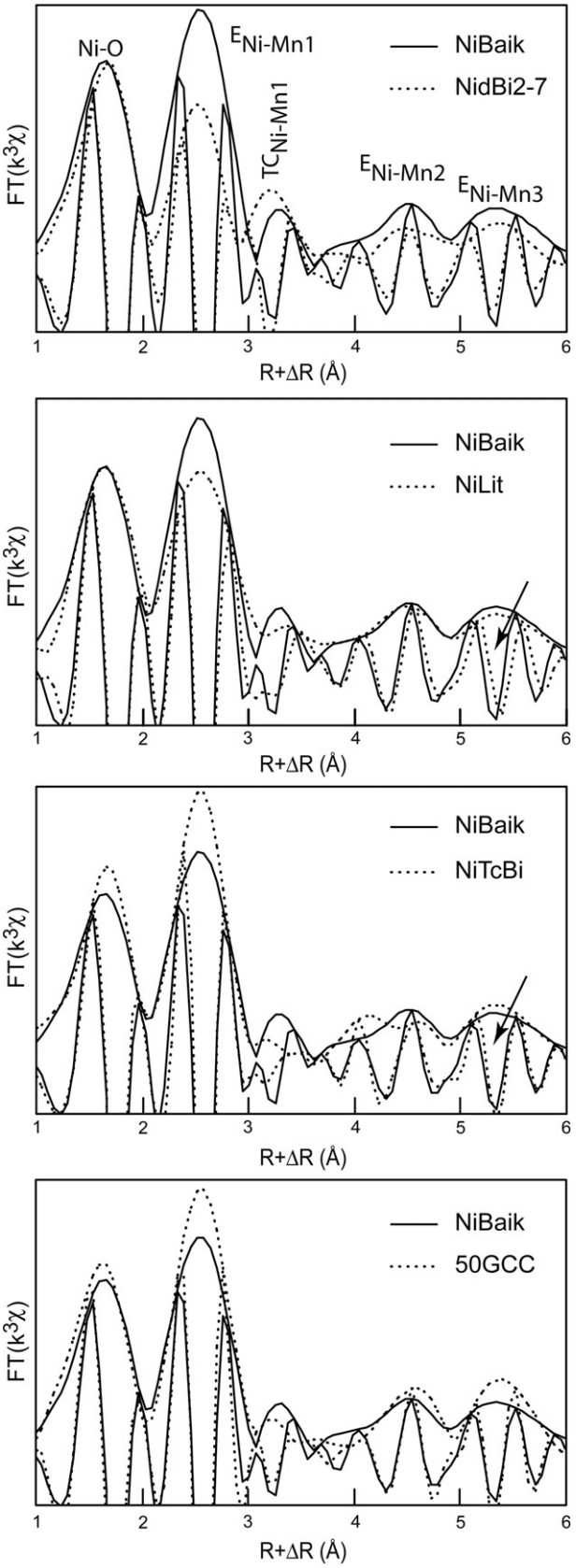

Fig. 7. Fourier transforms (FTs) of the Ni-EXAFS data in Fig. 6. The shift in frequency observed in the [5–7 $Å^{-1}$] k interval in Fig. 6 transforms in the real space as a phase difference of the imaginary parts of the Ni–Mn1 and Ni–Mn3 peaks. The phase difference increases with the radial distance.

(Fig. 4). With a cation ionic potential (valency over ionic radius) of only 0.72, compared to 2.0 for Ca, K has a low affinity for water and usually occurs in dehydrated to weakly hydrated interlayers (Ferrage et al., 2005). Consequently, the 1W crystallites in 2W–1W vernadite are probably K-rich and nearly homoionic given the narrowness of their 0 0 1 reflection. Also, the proportion of 2W and 1W layers in mixed-layer crystallites should depend on the Ca/K ratio and, thus, no two crystallites are likely to be chemically and structurally identical, in agreement with diffraction data. However, it is not possible to conclude whether the proportion of 2W and 1W layers in a given crystallite varies with the hydration state of the sample because the stability of the 2W layers with relative humidity is unknown. XRD analysis of the bulk sample is inconclusive about this question because the 2W–1W vernadite specimen is minor.

3.3. EXAFS spectroscopy

3.3.1. Mn K-edge EXAFS

Mn K-edge EXAFS spectroscopy is sensitive to Mn oxidation state, Mn–O and Mn–Mn interatomic distances, and polyhedral connectivity (Manceau and Combes, 1988). Therefore, it complements the mineralogical and structural information obtained from XRD. Micro-EXAFS spectra were recorded at the same POIs as for μ-XRD. The Mn-EXAFS spectra from the Ba-rich and Ni-rich layers are distinct, although each set of spectra from the same chemical type of layer is statistically invariant. The distinction can be seen in the spectral shapes in the [7.0–9.5 $Å^{-1}$] interval and confirms the existence of two separate manganese species (Fig. 5a). There is, however, a similarity in the frequency of all spectra from both species, indicating that the average Mn oxidation state is similar throughout the sample. The [7.0–9.5 $Å^{-1}$] region, also called the 'indicator region' (Marcus et al., 2004a), is sensitive to the amount and ordering of Mn^{4+} and Mn^{3+} in the manganese layer of phyllomanganate and the size of the tunnel structure in tectomanganate (Manceau et al., 2002a, 2004, 2005; Gaillot et al., 2003). The form of Mn in the two manganates was determined using spectra of model compounds as structural fingerprints. A selection of candidate species is shown in Fig. 5, and includes a synthetic turbostratic birnessite, $Na_{0.24}(H_2O)_{0.72}(Mn^{4+}_{0.94}Vac_{0.06})O_2$ (dBi, Marcus et al., 2004a; Villalobos et al., 2006); a synthetic hexagonal birnessite, $K_{0.231}Mn^{3+}_{0.077}(Mn^{4+}_{0.885}Vac_{0.115})O_2 \cdot 0.60H_2O$, made from $KMnO_4$ (KBi$_8$, Gaillot et al., 2003); a synthetic hexagonal birnessite, $Mn^{2+}_{0.05}Mn^{3+}_{0.12}(Mn^{4+}_{0.74}Mn^{3+}_{0.10}Vac_{0.17})O_{1.7}(OH)_{0.3}$ (HBi), prepared by equilibrating at low pH triclinic Na-birnessite, $Na_{0.31}(Mn^{4+}_{0.69}Mn^{3+}_{0.31})O_2 \cdot 0.40H_2O$ (TcBi, Silvester et al., 1997); and, a synthetic lithiophorite (Lit, Yang and Wang, 2003). TcBi and Lit have about the same proportion of layer Mn^{3+}, but not the same Mn^{4+}-Mn^{3+} cation ordering (Drits et al., 1997; Manceau et al., 2005). The best spectral match to our Mn oxide database of the Ni-containing manganate (MnBaik_Ni) was obtained with dBi, which has no Mn^{3+} and no interlayer Mn (Fig. 5b). In MnBaik_Ni, vacant octahedral sites (Vac) are capped likely by interlayer Ca since the lake water is rich in calcium bicarbonate, and Ca is difficult to detect as a backscatterer by Mn-EXAFS.

The spectrum of the Mn species from the Ba-rich layers (MnBaik_Ba) more closely resembles the romanechite spectrum than any other references (Fig. 5g). The MnBaik_Ba spectrum is clearly different from that of hollandite, a 2×2 tunnel structure tectomanganate, and slightly different from that of todorokite. Upon decreasing the size of the tunnel in tectomanganates, the second oscillation broadens and eventually splits into two maxima at 6.5 and 6.8 $Å^{-1}$, as

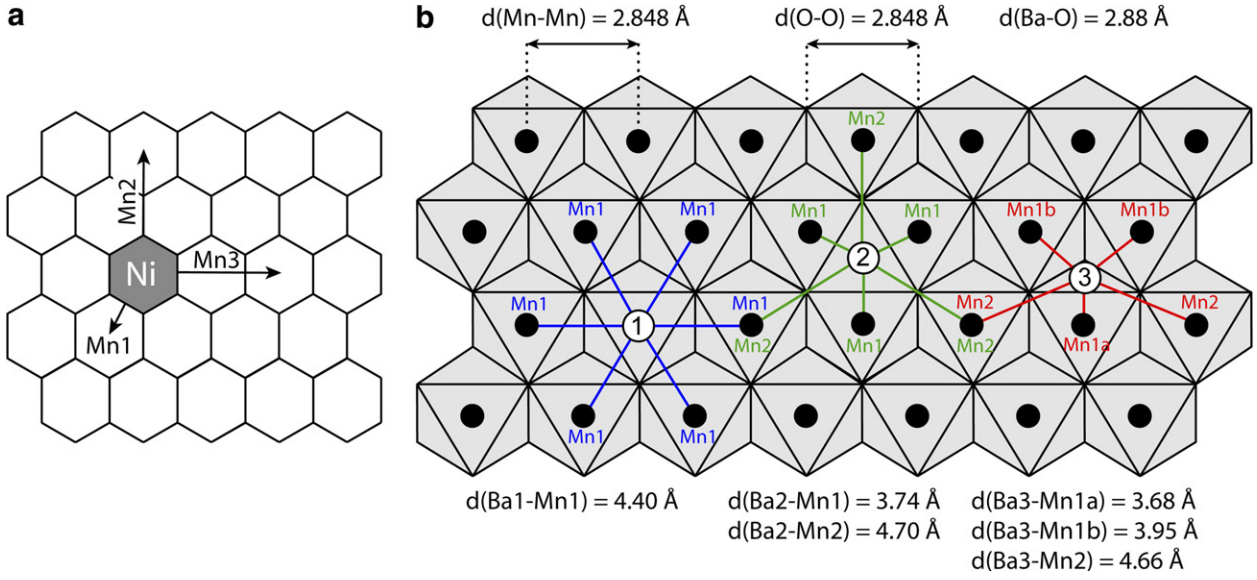

Fig. 8. (a) Representation of the ^{E}Ni–Mn1, ^{E}Ni–Mn2, and ^{E}Ni–Mn3 pairs in a phyllomanganate layer with $a = b = 2.848$ Å (HBi). Theoretical sorption sites of Ba in the interlayer of a phyllomanganate. At position 1 (Ba1), Ba is above a vacant layer site and is corner-linked to six Mn octahedra from the layer. At position 2 (Ba2), Ba is at the center of a tetrahedral site formed by three edge-sharing Mn octahedra, and is linked to them by corners. At position 3 (Ba3), Ba is shifted from the previous position in direction of one of the three edge-sharing Mn octahedra by 1/4 the Ba2–Mn1 distance.

observed in Fig. 5i and j for hollandite and pyrolusite, an 1×1 tunnel structure tectomanganate (Manceau and Combes, 1988). Thus, the shape of the second oscillation is sensitive to the proportion of edge- and corner-sharing Mn octahedra in manganates, being symmetrical in the absence of corner-sharing linkage, and otherwise asymmetrical. In phyllomanganates, the width of the second oscillation is indicative of interlayer Mn octahedra linked through corners to layer Mn octahedra (Manceau et al., 1997), as shown in Fig. 5d with HBi which has 17% interlayer Mn. From the comparison of MnBaik_Ni and KBi_8 (Fig. 5c), the maximum amount of interlayer Mn in the Lake Baikal sample is estimated to be 8%.

3.3.2. Ni K-edge EXAFS

Since nickel is always sixfold coordinated in phyllomanganates, the shape and frequency of Ni-EXAFS essentially depend upon the type (e.g., Ni vs. Mn) and position (e.g., layer vs. interlayer) of non-nearest-neighbor atoms, leading to the concept of a 'structure fingerprint', as for Mn-EXAFS (Manceau et al., 2007). From the survey of about fifteen reference spectra from layer Ni oxides representing a range of Ni binding environments, four were selected for a demonstration of the fingerprint technique applied to Ni speciation and uniqueness of our structural interpretation (Fig. 6). The NidBi2-7 reference is a synthetic turbostratic birnessite (dBi) containing a total of 0.002 Ni per Mn atom, of which 45% are substituted for Mn in the layer (^{E}Ni complex neighbored by six Mn^{4+}), and 55% are in the interlayer at vacant Mn layer site (^{TC}Ni complex; Manceau et al., 2007). The NiTcBi reference is a triclinic sodium birnessite (TcBi) doped with 0.0044 Ni per Mn. The NiLit reference is a natural Ni-containing lithiophorite (Manceau et al., 2002b). Finally, the 50GCC reference is a marine Mn^{4+} 10Å-vernadite from the Costa Rica margin. This reference has only ^{E}Ni (Bodei et al., 2006), as do NiTcBi and NiLit.

The Ni-EXAFS spectral shape of the Lake Baikal sample (NiBaik) is similar to those of NiTcBi, NiLit and 50GCC, and distinct from that of NidBi2-7, suggesting that Ni is predominantly incorporated in the Mn layer of the Baikal sample. The split second oscillation has the same frequency for 50GCC and NiBaik, and is shifted to lower k values for NiTcBi, and even more so for NiLit. The increase of the EXAFS frequency in the two Mn^{3+}-containing references arises because the ^{E}Ni–Mn^{3+} distances are longer than the ^{E}Ni–Mn^{4+} distances. Supporting evidence is seen by comparing the Fourier transforms (FTs), which shows that the imaginary part of the ^{E}Ni–Mn3 peak, and to a lesser extent of the ^{E}Ni–Mn1 peak, is shifted to higher distance in NiTcBi and NiLit relative to NiBaik (Fig. 7). The ^{E}Ni–Mn3 pair is more sensitive to the presence of Mn^{3+} around Ni because the distance separation between ^{E}Ni and Mn3 is twice that of ^{E}Ni and Mn1 (Fig. 8a). Thus, we conclude that Ni is surrounded only by Mn^{4+} atoms in NiBaik, in agreement with the lack of layer Mn^{3+} deduced from XRD and Mn-EXAFS data. The FT of NiBaik seems to have a peak at $R + \Delta R = 3.2$–3.3 Å, which suggests the occurrence of some ^{TC}Ni atoms in the interlayer. Data simulations showed that the proportion of ^{TC}Ni to total Ni is less than 10%, which is consistent with the high amplitude of the ^{E}Ni–Mn1 peak.

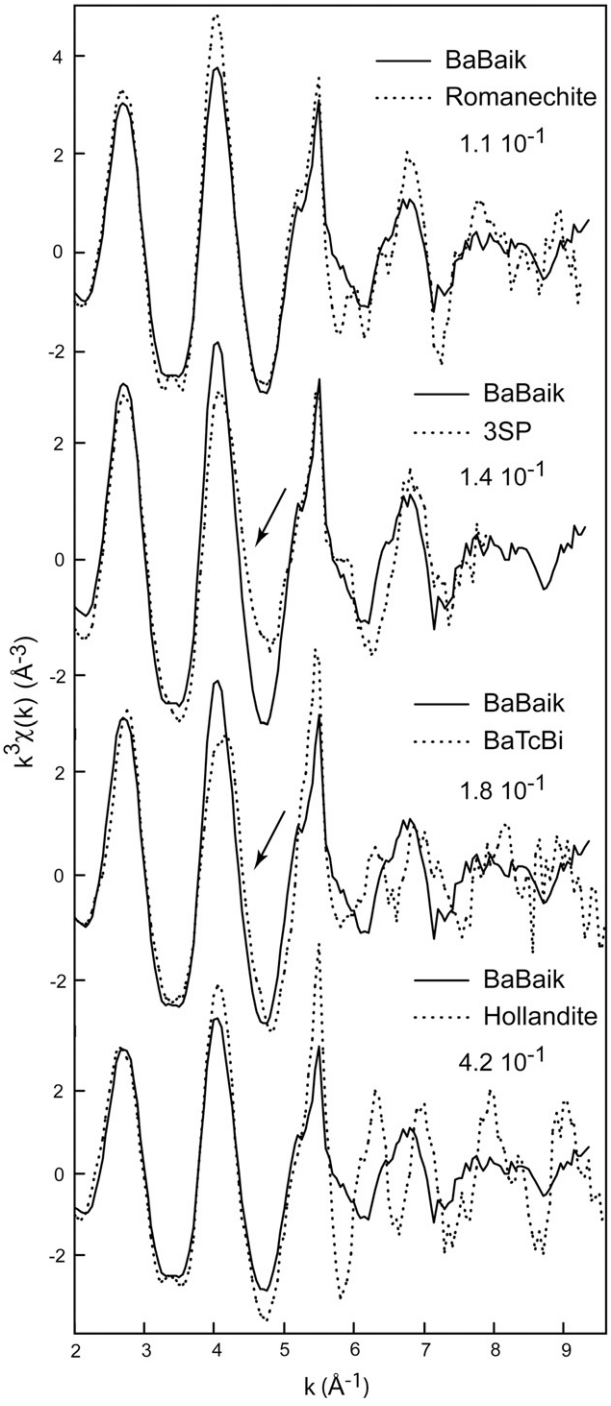

Fig. 9. Ba L_3-edge EXAFS spectrum of the sample (BaBaik, solid line) and references (dotted lines). The closest match of BaBaik is with romanechite, in agreement with μ-XRD data. The sharp peak at 5.5 $Å^{-1}$ is a multi-electronic effect, which does not affect the quantitative analysis and structural interpretation (Manceau et al., 2007). The Norm. Sum-Sq values were calculated over the [2.0–8.0 $Å^{-1}$] k interval.

3.3.3. Ba L_3-edge EXAFS

Four references were used to determine Ba speciation: hollandite from Langenberg, Germany (Frondel et al.,

Table 1
Results from quantitative analysis of the Ba L_3-Edge EXAFS data

Sample	Ba–O			Ba–Mn1			Ba–Mn2			ΔE	Res
	R (Å)	CN	σ (Å)	R (Å)	CN	σ (Å)	R (Å)	CN	σ (Å)		
Hollandite[a]	2.90	8.0[b]	0.13	3.68	4.0[b]	0.12	4.66	8.0[b]	0.13	4.0	9.3
				4.00	8.0[b]	0.17					
Romanechite	2.89	8.0[b]	0.13	3.76	2.0[b]	0.13	4.70	4.0[b]	0.13	2.9	13.7
				3.95	4.0[b]	0.17					
BaTcBi	2.85	6.0[b]	0.13	3.62	1.0[b]	0.09	4.68	2.0[b]	0.11	1.9	14.1
				4.08	2.0[b]	0.16					
3SP	2.85	5.3	0.13	3.68	1.0[b]	0.06	3.72	2.0[b]	0.12	2.6	11.2
				3.92	2.0[b]	0.10					
BaBaik	2.88	8.8	0.16	3.84	1.0	0.13	4.67	1.5	0.13	2.2	14.6

ΔE, inner potential correction in eV; Res, fit residual defined as $\sum\{|\chi_{exp} - \chi_{fit}|\}/\sum\{|\chi_{exp}|\}$; interval of the inverse Fourier transform: 1.05–3.6 Å; $sS_0^2 = 1.4$; CN and σ values in BaBaik are not individually accurate because these two parameters were highly correlated in the spectral fit.
[a] Crystallographic values are: 8 O at 2.88–2.90 Å, 4 Mn at 3.58–3.65 Å, 8 Mn at 3.99–4.17 Å, and 8 Mn at 4.59–4.64 Å (Miura, 1986).
[b] Fixed value.

1960), romanechite from Hufgard quarry, Germany, Ba-sorbed synthetic TcBi (BaTcBi) and a natural Ba-containing vernadite (3SP). The purity and crystallinity of the three first standards were verified by XRD. The last reference is from quartz coatings, as the 6KR phyllomanganate reference described in the XRD section. In all these references, Ba is located above an empty tetrahedral cavity formed by three edge-sharing MnO_6 octahedra, and off-centered toward one of the three O_{layer}–O_{layer} edges to an extent that depends on the mineral species (Fig. 8b; Manceau et al., 2007). When the offset in position is important, the first Mn shell is split, which manifests itself in the EXAFS spectrum by a split of the fourth oscillation at 6.0–7.5 $Å^{-1}$, as observed for hollandite and BaTcBi (Fig. 9; Table 1). This oscillation has a single maximum in the two other references and BaBaik, meaning that Ba is closer to the center of the tetrahedral cavity. The exact shape of this oscillation also depends to some extent on the Ba–O distance (or Ba coordination) since the Ba–O wave interferes with the Ba–Mn waves in this spectral region. Thus, care has to be taken when drawing fine structural distinctions based solely on the shape of the fourth oscillation. The distance separation between the two Mn subshells determined by data simulation is $4.08 - 3.62 = 0.46$ Å in BaTcBi, $4.00 - 3.68 = 0.32$ Å in hollandite, $3.92 - 3.68 = 0.24$ Å in 3SP, and $3.95 - 3.76 = 0.19$ Å in romanechite (Electronic Annex EA-6). The BaBaik data could be reproduced with an unsplit first Mn shell at 3.84 Å, suggesting that of all manganate species examined here, Ba is the closest to the center of the tetrahedral cavity in BaBaik. The specificity of the Ba environment in BaBaik also is seen clearly on the Fourier transforms (Fig. 10).

The plausibility of our fit models was verified by constructing an idealized MnO_2 octahedral sheet and calculating by geometry alone the Ba–Mn distances for Ba at the center of the tetrahedral cavity (Ba2 position), and shifted in the direction of the nearest Mn shell by 1/4 the Ba2–Mn1 distance (Ba3 position, Fig. 8b). In this model, the unsplit Mn1 shell is at 3.74 Å, and the second-nearest Mn shell (Mn2) at 4.70 Å from Ba2. The split Mn1 shell is at 3.68 and 3.95 Å, and the Mn2 shell at 4.66 Å from Ba3. These theoretical values are in good agreement with EXAFS distances (Table 1) and support our structural interpretation.

Data simulation also showed that the phase and amplitude of the second EXAFS oscillation are sensitive to Ba coordination, which is right-shifted (i.e., shorter Ba–O distance) and less intense when Ba is sixfold (BaTcBi, 3SP) coordinated than when it is coordinated to eight or more oxygens (hollandite, romanechite; Fig. 9). Using the wave frequency criterion, Ba is at least eight coordinated in the Lake Baikal sample, as confirmed by the similarity of the mean Ba–O distance in BaBaik and romanechite (2.88–2.89 Å; Table 1). The short Ba–O distance (2.85 Å) in phyllomanganate is also an indication that Ba is closer to the Mn layer when the structure is lamellar. Here, the wave amplitude criterion is less conclusive because simulations showed that high structural disorder occurs at the Ba site in BaBaik. In conclusion, Ba is associated with romanechite, but is bonded to a slightly different surface site than in the well-crystallized reference. In addition to the difference in crystallinity, it is possible that the two romanechite specimens do not have the same stoichiometry, with the Lake Baikal species containing less Mn^{3+} and more Mn vacancies since the lake sediment–water interface is oxidizing. This hypothesis is supported by the compositional variability of todorokite. Two structural formulae for natural todorokite have been reported in the literature: $Mg^{2+}_{0.07}Na^{+}_{0.06}Ca^{2+}_{0.03}\ K^{+}_{0.01}[Mn^{4+}_{0.80}Mn^{3+}_{0.17}Vac_{0.02}Fe^{3+}_{0.01}Al^{3+}_{0.01}]O_2 \cdot 0.55H_2O$ (Gutzmer and Beukes, 2000) and $Mg^{2+}_{0.07}\ Na^{+}_{0.07}\ Ca^{2+}_{0.02}K^{+}_{0.02}[Mn^{4+}_{0.73}Mn^{3+}_{0.27}]O_2 \cdot 0.7H_2O$ (Post et al., 2003). The specimen analyzed by Gutzmer and Beukes (2000) had a higher Mn^{4+}/Mn^{3+} ratio and probably contained some vacancies (Vac).

4. DISCUSSION

Dissolved (<0.45 μm) Ni concentrations in waters of Lake Baikal are about 2 nM while riverine inputs are up to 8 nM (Falkner et al., 1997). Nutrient-like vertical profiles and a flow-weighted mean residence time of 110 years, which is one-third of the mean water residence time, indicate an active removal process as a result of biological

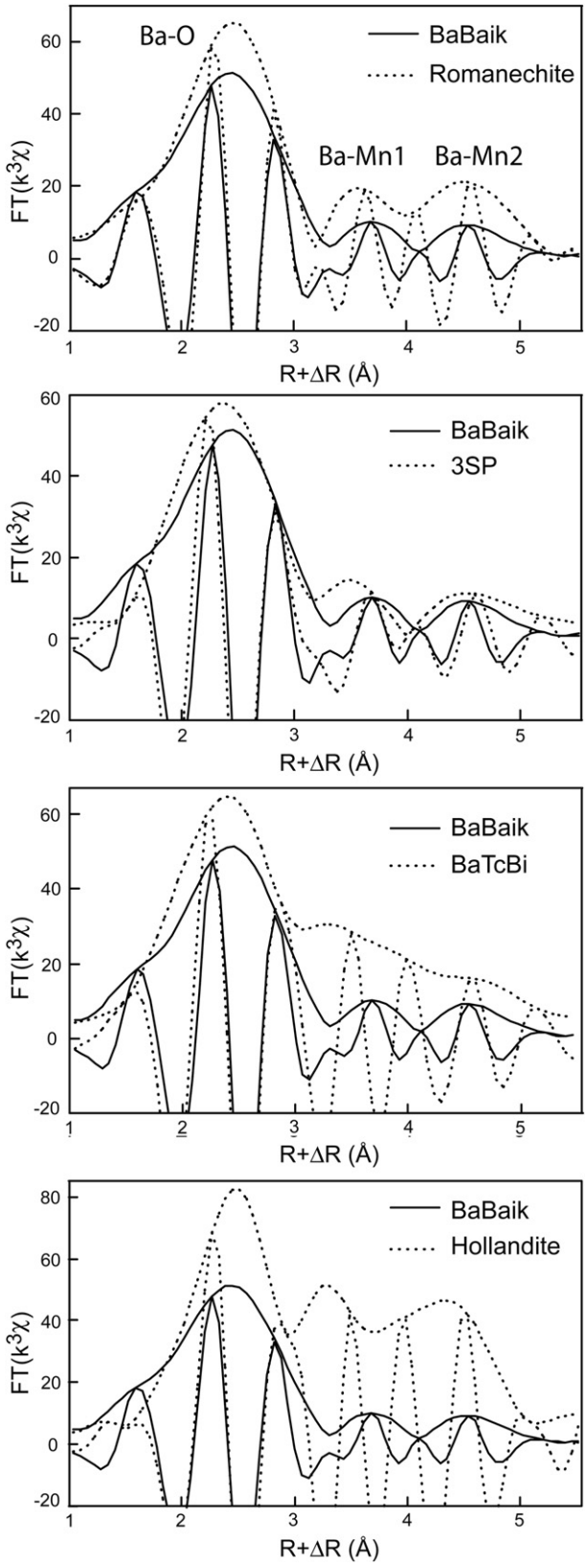

Fig. 10. Fourier transforms of Ba-EXAFS data in Fig. 9. Note the shift to higher $R + \Delta R$ values of the Ba–Mn1 peak position and phase for BaBaik relative to romanechite.

scavenging. Barium concentrations are about 70 nM (Falkner et al., 1997), comparable to other freshwater lakes with values between 30 and 300 nM (Sugiyama et al., 1992). Since the sulfate concentration is only about 50 μM, the Ba concentration is at a minimum two orders of magnitude undersaturated with respect to the solubility product of $BaSO_4$. Nonetheless, the vertical profile of Ba concentration is slightly depleted (10 nM) near the sediment–water interface, probably as a result of Ba scavenging by Mn nodules (Falkner et al., 1997). The mean flow-weighted residence time of Ba is in the same order as that of water, but a yet unknown amount of Ba may originate also from hydrothermal water discharge, such as that reported at Frolikha Bay, Northern Baikal (Kipfer et al., 1996). Barium concentrations of up to 2 μM controlled by barite solubility were measured in porewaters sampled at Frolikha Bay (Granina et al., 2007).

Although hydrothermal vent activity has not yet been discovered at the B.Ushkanii Island site, some indirect evidence exists. The site is located at crossing faults, and bottom waters from this site have enhanced electrical conductivity (Bukharov and Fialkov, 1996). Moreover, both diverse benthic organisms with new taxons and the hydrothermal precipitate geyserite were observed at this site just as at the Frolikha vent (Takhteev et al., 2001). If present, the hydrothermal activity would be responsible for an enhanced supply of Ba, and its precipitation at some distance from the source as high Ba-containing romanechite. The formation of this mineral is probably driven by the enhanced input of Ba, as this element acts as structure-directing template for the formation of 2×2 and 2×3 tectomanganates (Giovanoli and Balmer, 1983; Feng et al., 1998). Romanechite forms preferentially to hollandite at ambient condition because the size of the hydrated Ba^{2+} ion matches the dimension of the 2×3 tunnel of romanechite. In contrast, at higher temperature the 2×2 tunnel structure of hollandite is stabilized by anhydrous Ba.

The nickeliferous vernadite is probably not hydrothermal because it would be mixed with romanechite (i.e., their formation would be synchronous). It results more likely from the diagenetic transformation of hydrogeneous ferromanganese oxides. A diagenetic rather than hydrogenetic origin is supported by the low Fe/Mn ratio of the Ni-rich layers and the high intensity of the two XRD basal reflections, two characteristics that distinguish chemically and structurally vernadite from Fe-vernadite, the main Mn phase from hydrogeneous ferromanganese oxides (Takahashi et al., 2007). According to this interpretation, the romanechite layers would form episodically in response to the activity of hydrothermal plumes superimposed on a steady-state system, in which Ni-rich phyllomanganate layers continuously form by the hydrogenous—early diagenetic process. This scenario is compatible with the existence of Ba-rich, Ni-poor layers because hydrogenetic and diagenetic ferromanganese oxides have a much slower growth rate than hydrothermal oxides (Dymond et al., 1984; Halbach et al., 1988; Takematsu et al., 1989). Therefore, the amount of Ni incorporated from the lake water during the time span of the formation of a Ba-rich hydrothermal layer would be small.

In conclusion, the data support the existence of a subaquatic hydrothermal discharge at the nodule sampling spot of B. Ushkanii Island. The intermittent activity of venting episodes on that spot is recorded in the thus analyzed ferromanganese nodule by its particular but not uncommon zoned mineralogy and chemistry. For example, a similar bi-phasic manganate mineral association and Ba enrichment in romanechite has been found recently in shallow submarine sediments vented by diffuse hydrothermal seepage of water at Bahia Concepcion, Baja California Sur, Mexico (Canet et al., 2005). Here, the area of suspicion for venting could be ascertained once other nodules become available. At present, the exploration of the lake-bottom sediment is made difficult by the lack of submarine research logistics at Lake Baikal.

ACKNOWLEDGMENTS

We thank A.A. Bukharov for providing the nodule sample. G. Schmidt assisted during XAS measurements at the ALS beamline 10.3.2. We also gratefully acknowledge A.P. Hammersley of the ESRF for making the Fit2d code available. The final version of the manuscript benefited from the careful reviews by two anonymous referees. The ALS is supported by the Director, Office of Energy Research, Office of Basic Energy Sciences, Materials Sciences Division of the US Department of Energy, under Contract No. DE-AC02-05CH11231.

APPENDIX A. SUPPLEMENTARY DATA

Supplementary data associated with this article can be found, in the online version, at doi:10.1016/j.gca.2007.02.007.

REFERENCES

Amirzhanov B. J., Pampoura V. D., and Piskunova L. F. (1993) Rare elements in the Lake Baikal ferromanganese nodules. *IPPCCE Newsl.* **7**, 25–28.

Bodei, S., Buatier, M., and Manceau, A. (2006) Mn and Ni speciation in metalliferous oceanic oxides (XRD, EXAFS and TEM studies). In: *Joint Meeting of The Clay Minerals Society and the French Clay Group, June 3–7*. Journal of Conference Abstracts 45.

Brindley G. W., and Brown G. (1980) *Crystal structures of clay minerals and their X-ray identification*. Mineralogical Society, London.

Bukharov A. A., and Fialkov V. A. (1996) The geological structure of bottom in Baikal. *Nauka, Novosibirsk*, 117 (in Russian).

Bukharov A. A., Murashko D. N., and Fialkov V. A. (1992) Ferromanganese concretions on the underwater slope of Ushkanii Island (Lake Baikal). *Geologiya i Geofizika* **1**, 22–29 (in Russian).

Burns R. G., and Burns V. M. (1979) Manganese oxides. In *Marine Minerals*, vol. 6 (ed. R. G. Burns). Mineralogical Society of America, pp. 1–46.

Callender E., and Granina L. (1992) Transition metal geochemistry of sedimentary pore fuids associated with hydrothermal activity in Lake Baikal. In *Proceedings of Water–Rock Interaction WRI-7* (eds. Y.K. Kharaka and A.S. Maest). Balkema, Rotterdam, pp. 621–626.

Canet C., Prol-Ledesma R. M., Proenza J. A., Rubio-Ramos M. A., Forrest M. J., Torres-Vera M. A., and Rodriguez-Diaz A. A. (2005) Mn–Ba–Hg mineralization at shallow submarine hydrothermal vents in Bahia Concepcion, Baja California Sur, Mexico. *Chem. Geol.* **224**, 96–112.

Crane K., Hecker B., and Golubev V. (1991) Hydrothermal vents in Lake Baikal. *Nature* **350**, 281.

Deike R. G., Granina L., Callender E., and McGee J. J. (1997) Formation of ferric iron crusts in quaternary sediments of Lake Baikal, Russia, and implications for paleoclimate. *Mar. Geol.* **139**, 21–46.

Drits V. A., and Tchoubar C. (1990) *X-ray Diffraction by Disordered Lamellar Structures: Theory and Applications to Microdivided Silicates and Carbons*. SpringerVerlag, Berlin.

Drits V. A., Silvester E., Gorshkov A. I., and Manceau A. (1997) The structure of synthetic monoclinic Na-rich birnessite and hexagonal birnessite. Part 1. Results from X-ray diffraction and selected area electron diffraction. *Am. Mineral.* **82**, 946–961.

Dymond J., Lyle B., Finney B., Piper D. Z., Murphy K., Conard R., and Pisias N. (1984) Ferromanganese nodules from MANOP sites H, S, and R – control of mineralogical and chemical composition by multiple accretionary processes. *Geochim. Cosmochim. Acta* **48**, 931–949.

Falkner K. K., Measures C. I., Herbelin S. E., Edmond J. M., and Weiss R. F. (1997) Minor and trace element chemistry of Lake Baikal, its tributaries, and surrounding hot springs. *Limnol. Oceanogr.* **42**, 329–345.

Feng Q., Yanagisawa K., and Yamasaki N. (1998) Hydrothermal soft chemical process for synthesis of manganese oxides with tunnel structures. *J. Porous Mater.* **5**, 153–161.

Ferrage E., Lanson B., Sakharov B. A., and Drits V. A. (2005) Investigation of smectite hydration properties by modeling experimental X-ray diffraction patterns: Part I. Montmorillonite hydration properties. *Am. Mineral.* **90**, 1358–1374.

Frondel C., Marvin U. B., and Ito J. (1960) Notes and News: new data on birnessite and hollandite. *Am. Mineral.* **45**, 871–875.

Gaillot A. C., Flot D., Drits V. A., Burghammer M., Manceau A., and Lanson B. (2003) Structure of synthetic K-rich birnessites obtained by high-temperature decomposition of $KMnO_4$. I. Two-layer polytype from a 800 °C experiment. *Chem. Mater.* **15**, 4666–4678.

Gaillot A. C., Drits V. A., Manceau A., and Lanson B. (2007) Structure of the synthetic K-rich phyllomanganate birnessite obtained by high-temperature decomposition of $KMnO_4$: substructures of K-rich birnessite from 1000 °C experiment. *Micro. Meso. Mater.* **98**, 267–282.

Gebruk A. (1995) Hydrothermal vents in Lake Baikal: large input of methane carbon into the surrounding biota. *Deep-Sea Newsl.* **23**, 15–17.

Giovanoli R., and Balmer B. (1983) Darstellung und Reaktionen von Psilomelan (Romanéchit) $Ba_2Mn_{15}O_{30}\cdot 4H_2O$. *Chimia* **37**, 424–427.

Giovanoli R., and Bürki P. (1975) Comparison of X-ray evidence of marine manganese nodules and non-marine manganese ore deposits. *Chimia* **29**, 266–269.

Giovanoli R., Bürki P., Giuffredi S., and Stumm W. (1975) Layer structured manganese oxide hydroxides IV: the buserite groups; structure stabilization of transition elements. *Chimia* **29**, 517–520.

Giovanoli R., Stähli E., and Feitknecht W. (1970) Über oxidhydroxide des vierwertigen mangans mit schichtengitter. 2. Mangan(III)–manganat(IV). *Helv. Chim. Acta* **53**, 454–464.

Golubev V. A., Klerkx J., and Kipfer R. (1993) Heat flow, hydrothermal vents and static stability of discharging thermal water in Lake Baikal (south-eastern Siberia). *Bull. Centr. Rech. Explor.-Prod. Elf Aquitaine* **17**, 53–65.

Granina L. (1992a) Ferromanganese formations in Lake Baikal: formation conditions, composition, distribution. *IPPCCE Newsl.* **6**, 39–47.

Granina L. (1992b) Vertical profiles of iron and manganese concentration in Baikal interstitial solutions. *Geochem. Int.* **29**, 132–139.

Granina L., Klerkx J., Callender E., Leermakers M., and Golobokova L. P. (2007) Peculiarities of the bottom sediments and porewaters in the area of hydrothermal venting in Lake Baikal (Frolikha Bay). *Russ. Geol. Geophys.* **3**, 305–316.

Granina L., Müller B., and Wehrli B. (2004) Origin and dynamics of Fe- and Mn-sedimentary layers in Lake Baikal. *Chem. Geol.* **205**, 55–72.

Granina L., Müller B., Wehrli B., and Martin P. (2000) Oxygen, iron, and manganese at the sediment–water interface in Lake Baikal. *Terra Nostra* **9**, 87–94.

Granina L. Z., Callender E., Mats V. D., and Golobokova L. P. (2002) On deep circulation of meteoric waters within the Baikal Rift. *EGU Stephan Mueller Special Publ. Ser.* **2**, 161–170.

Gutzmer J., and Beukes N. J. (2000) Asbestiform manjiroite and todorokite from the Kalahari manganese field, South Africa. *South African J. Geol.* **103**, 163–174.

Halbach P., Friendrich G., and von Stackelberg U. (1988) *The Manganese Nodule Belt of the Pacific Ocean*. Enke, Stuttgart.

Hammersley A. P., Svensson S. O., Han M., Fitch A. N., and Hausermann D. (1996) Two-dimensional detector software: from real detector to idealised image or two-theta scan. *High Pressure Res.* **14**, 235–248.

Jones B. F., and Bowser C. J. (1978) Mineralogy and chemistry of limnetic sediments. In *Lakes Chemistry, Geology, Physics* (ed. A. Lerman). Springer-Verlag.

Kipfer R., Aeschbach-Hertig W., Hofer M., Hohmann R., Imboden D. M., Baur H., Golubev V., and Klerkx J. (1996) Bottomwater formation due to hydrothermal activity in Frolikha Bay, Lake Baikal, eastern Siberia. *Geochim. Cosmochim. Acta* **60**, 961–971.

Lanson B., Drits V. A., Silvester E. J., and Manceau A. (2000) Structure of H-exchanged hexagonal birnessite and its mechanism of formation from Na-rich monoclinic buserite at low pH: new data from X-ray diffraction. *Am. Mineral.* **85**, 826–835.

Leybovich L. Z. (1983) Iron and manganese in oxidized Baikal sediments. *Geochem. Int.* **21**, 47–53.

Manceau A., and Combes J. M. (1988) Structure of Mn and Fe oxides and oxyhydroxides: a topological approach by EXAFS. *Phys. Chem. Mineral.* **15**, 283–295.

Manceau A., Drits V. A., Silvester E., Bartoli C., and Lanson B. (1997) Structural mechanism of Co(II) oxidation by the phyllomanganate, Na-buserite. *Am. Mineral.* **82**, 1150–1175.

Manceau A., Gorshkov A. I., and Drits V. A. (1992) Structural chemistry of Mn, Fe, Co, and Ni in Mn hydrous oxides. II. Information from EXAFS spectroscopy, electron and X-ray diffraction. *Am. Mineral.* **77**, 1144–1157.

Manceau A., Lanson M., and Geoffroy N. (2007) Natural speciation of Ni, Zn, Ba and As in ferromanganese coatings on quartz using X-ray fluorescence, absorption, and diffraction. *Geochim. Cosmochim. Acta* **71**, 95–128.

Manceau A., Marcus M. A., and Tamura N. (2002a) Quantitative speciation of heavy metals in soils and sediments by synchrotron X-ray techniques. In *Applications of Synchrotron Radiation in Low-temperature Geochemistry and Environmental Science*, vol. 49 (eds. P.A. Fenter, M.L. Rivers, N.C. Sturchio, and S.R. Sutton). Mineralogical Society of America, pp. 341–428.

Manceau A., Marcus M. A., Tamura N., Proux O., Geoffroy N., and Lanson B. (2004) Natural speciation of Zn at the micrometer scale in a clayey soil using X-ray fluorescence, absorption, and diffraction. *Geochim. Cosmochim. Acta* **68**, 2467–2483.

Manceau A., Tamura N., Marcus M. A., MacDowell A. A., Celestre R. S., Sublett R. E., Sposito G., and Padmore H. A. (2002b) Deciphering Ni sequestration in soil ferromanganese nodules by combining X-ray fluorescence, absorption and diffraction at micrometer scales of resolution. *Am. Mineral.* **87**, 1494–1499.

Manceau A., Tommaseo C., Rihs S., Geoffroy N., Chateigner D., Schlegel M., Tisserand D., Marcus M. A., Tamura N., and Chen Z. S. (2005) Natural speciation of Mn, Ni and Zn at the micrometer scale in a clayey paddy soil using X-ray fluorescence, absorption, and diffraction. *Geochim. Cosmochim. Acta* **69**, 4007–4034.

Marcus M. A., MacDowell A. A., Celestre R., Manceau A., Miller T., Padmore H. A., and Sublett R. E. (2004a) Beamline 10.3.2 at ALS: a hard X-ray microprobe for environmental and materials sciences. *J. Synch. Rad.* **11**, 239–247.

Marcus M. A., Manceau A., and Kersten M. (2004b) Mn, Fe, Zn and As speciation in a fast-growing ferromanganese marine nodule. *Geochim. Cosmochim. Acta* **68**, 3125–3136.

Martin P., Granina L., Martens K., and Goddeeris B. (1998) Oxygen concentration profiles in sediment of two ancient lakes: Lake Baikal (Siberia, Russia) and Lake Malawi (East Africa). *Hydrobiologia* **367**, 163–174.

Miura H. (1986) The crystal structure of Hollandite. *Mineral. J.* **13**, 119–129.

Müller B., Granina L., Schaller T., Ulrich A., and Wehrli B. (2002) P, As, Sb, Mo, and other elements in sedimentary Fe/Mn layers of Lake Baikal. *Environ. Sci. Technol.* **36**, 411–420.

Post J. E., and Appleman D. E. (1994) Crystal structure refinement of lithiophorite. *Am. Mineral.* **79**, 370–374.

Post J. E., Heaney P. J., and Hanson J. (2003) Synchrotron X-ray diffraction of the structure and dehydration behavior of todorokite. *Am. Miner.* **88**, 142–150.

Proux O., Nassif V., Prat A., Ulrich O., Lahera E., Biquard X., Menthonnex J. J., and Hazemann J. L. (2006) Feedback system of a liquid-nitrogen-cooled double-crystal monochromator: design and performances. *J. Synch. Rad.* **13**, 59–68.

Reynolds, Jr., R. C. (1989) Diffraction by small and disordered crystals. In *Modern Powder Diffraction*, vol. 20 (eds. D.L. Bish and J.E. Post). Mineralogical Society of America, pp. 145–181.

Shanks I. W. C., and Callender E. (1992) Thermal springs in Lake Baikal. *Geology* **20**, 495–497.

Silvester E., Manceau A., and Drits V. A. (1997) The structure of synthetic monoclinic Na-rich birnessite and hexagonal birnessite. Part 2. Results from chemical studies and EXAFS spectroscopy. *Am. Mineral.* **82**, 962–978.

Sugiyama M., Hori T., Kihara S., and Matsui M. (1992) A geochemical study on the specific distribution of barium in Lake Biwa, Japan. *Geochim. Cosmochim. Acta* **56**, 597–605.

Takahashi Y., Manceau A., Marcus M. A., and Usui A. (2007) Chemical and structural control of the partitioning of Co, Ce, and Pb in marine ferromanganese oxides. *Geochim. Cosmochim. Acta* **71**, 984–1008.

Takematsu N., Sato Y., and Okabe S. (1989) Factors controlling the chemical composition of marine manganese nodules and crusts: a review and synthesis. *Marine Chem.* **26**, 41–56.

Takhteev V. V., Bukharov A. A., Proviz V. I., Sitnikova T. Y., and Galkin A. N. (2001) A peculiarity of bottom fauna within unusual geological environment of the northern slope of Bolshoi Ushkany Island (Lake Baikal). In *Studies of the Fauna in Waters Bodies of Eastern Siberia* (ed. V.V. Takhtaeev). Ikrutsk University (in russian), pp. 3–8.

Teo B. K. (1986) *EXAFS: Basic Principles and Data Analysis*. Springer-Verlag, Berlin.

Turner S., and Buseck P. R. (1979) Manganese oxide tunnel structures and their intergrowths. *Science* **203**, 456–458.

Turner S., and Post J. E. (1988) Refinement of the substructure and superstructure of romanechite. *Am. Mineral.* **73**, 1155–1161.

Usui A., and Mita N. (1995) Geochemistry and mineralogy of a modern buserite deposit from a hot spring in Hokkaido, Japan. *Clays Clay Mineral.* **43**, 116–127.

Varentsov I. M., Drits V. A., Gorshkov A. I., Sivtsov A. V., and Sakharov B. A. (1991) Me–Fe oxyhydroxide crusts from Krylov Seamount (Eastern Atlantic): mineralogy, geochemistry and genesis. *Marin. Geol.* **96**, 53–70.

Villalobos M., Lanson B., Manceau A., Toner B., and Sposito G. (2006) Structural model for the biogenic Mn oxide produced by Pseudomonas putida. *Am. Mineral.* **91**, 489–502.

Vodyanitskii Y. N., Lesovaya S. N., and Sivtsov A. V. (2003) Iron hydroxidogenesis in forest and steppe soils of the Russian Plain. *Eurasian Soil Sci.* **36**, 420–429.

Vodyanitskii Y. N., Vasilev A. A., Lesovaya S. N., Sataev E. F., and Sivtsov A. V. (2004) Formation of manganese oxides in soils. *Eurasian Soil Sci.* **37**, 572–584.

Votintsev, K. K. (1961) Hydrochemistry of Lake Baikal. *Izd. Akad. Nauk. SSSR* **357**. Database on website at www.nti.lin.irk.ru/bankzn/catalog.asp (in Russian).

Wadsley A. D. (1953) The crystal structure of psilomelane, (Ba, $H_2O)_2Mn_5O_{10}$. *Acta Crystallogr.* **6**, 433–438.

Yang D. S., and Wang M. K. (2003) Characterization and a fast method for synthesis of sub-micron lithiophorite. *Clays Clay Mineral.* **51**, 96–101.

Associate editor: Garrison Sposito

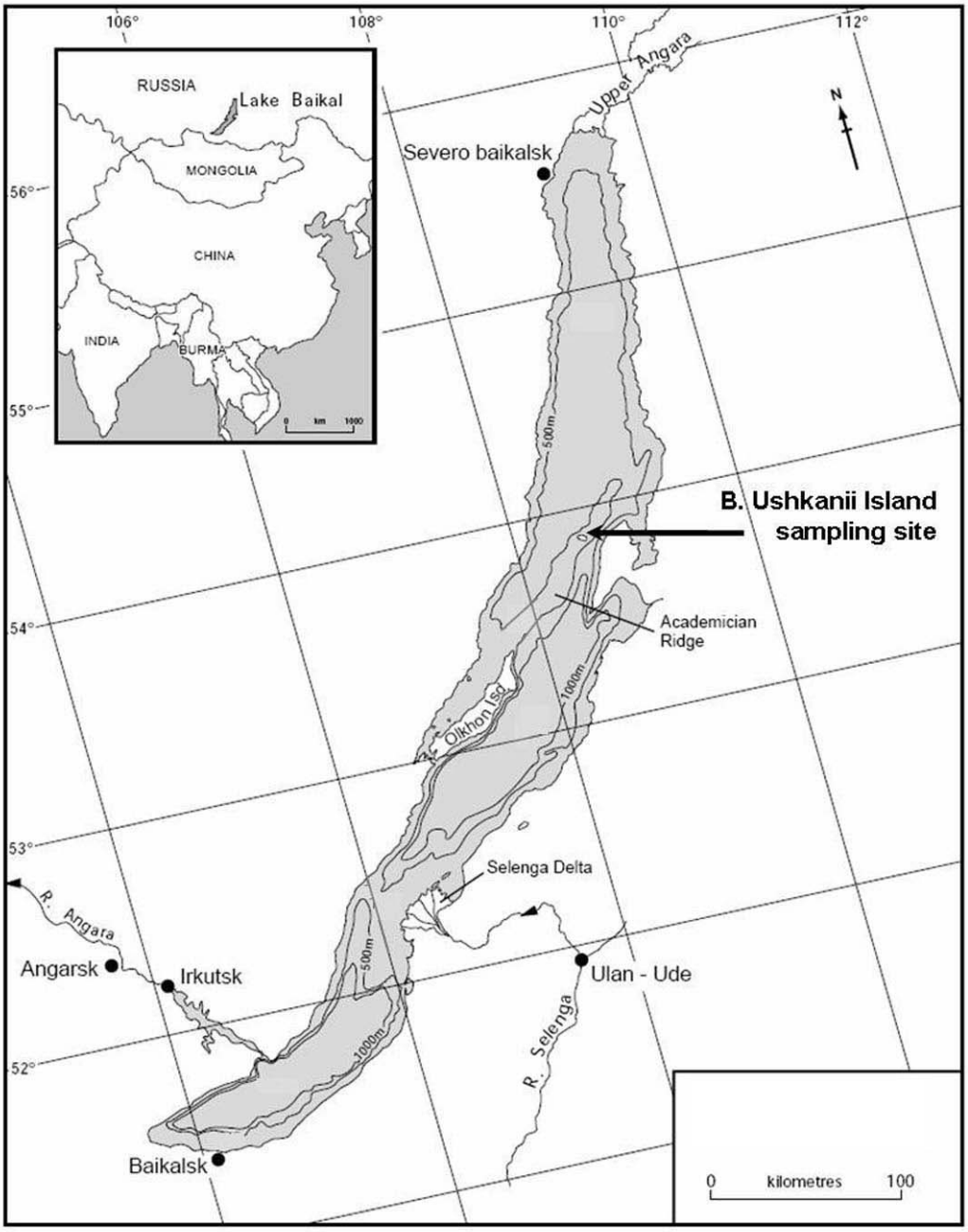

EA-1. Location of the ferromanganese nodule sampling site in Lake Baikal.

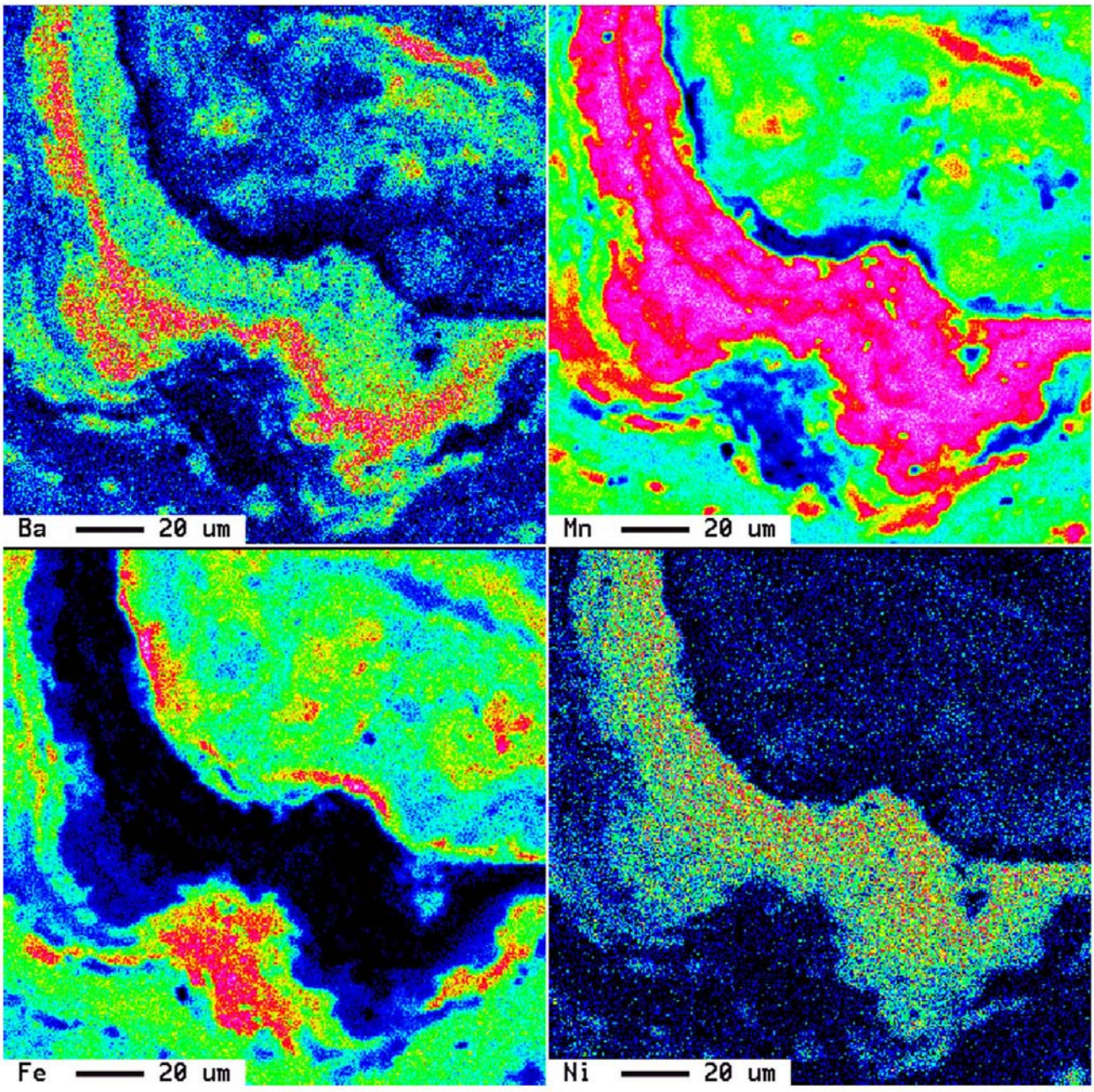

EA-2. Electron microprobe map of the distribution of Ba, Mn, Fe, and Ni in the ferromanganese nodule from Lake Baikal.

EA-3

Weight percent of major and minor elements from quantitative analyses by microprobe of 12 different spots from the map in EA-2

No.	MgO	Na_2O	K_2O	Fe_2O_3	BaO	Al_2O_3	SiO_2	TiO_2	NiO	P_2O_5	CaO	MnO	O	Total
1	0.31	0.07	0.24	21.17	4.45	4.39	5.63	0.38	0.25	1.52	2.19	32.70	-	73.31
2	0.41	0.07	0.35	17.39	4.77	5.47	6.91	0.53	0.35	1.56	2.45	37.12	-	77.38
3	0.57	0.03	0.17	30.31	2.00	6.42	6.71	0.36	0.45	1.98	2.28	25.65	-	76.94
4	0.63	0.07	0.12	7.23	6.66	1.45	0.85	0.19	1.08	0.53	2.84	53.73	-	75.37
5	0.25	0.07	0.11	14.87	1.98	3.67	4.51	0.12	0.20	1.20	1.21	17.57	-	45.77
6	0.31	0.09	0.08	22.26	2.65	5.37	3.49	0.15	0.33	1.46	1.57	24.81	-	62.57
7	0.21	0.01	0.03	25.88	1.76	5.07	3.64	0.12	0.23	2.06	1.50	20.41	-	60.92
8	0.28	0.04	0.06	57.30	0.75	3.76	5.50	0.09	0.09	3.01	1.65	8.35	-	80.87
9	0.66	0.03	0.17	7.76	5.46	0.91	1.05	0.16	1.20	0.54	3.48	52.82	-	74.22
10	0.80	0.11	0.18	7.60	3.08	1.34	0.94	0.14	1.41	0.48	3.39	45.46	-	64.93
11	0.19	0.02	0.03	37.90	0.94	2.59	5.13	0.18	0.06	2.13	1.88	15.15	-	66.21
12	0.32	0.17	0.11	39.15	0.70	3.15	7.06	0.12	0.22	1.75	1.81	12.54	-	67.10
Min	0.19	0.01	0.03	7.23	0.70	0.91	0.85	0.09	0.06	0.48	1.21	8.35	-	45.77
Max	0.80	0.17	0.35	57.30	6.66	6.42	7.06	0.53	1.41	3.01	3.48	53.73	-	80.87
Mean	0.41	0.07	0.14	24.07	2.93	3.63	4.29	0.21	0.49	1.52	2.19	28.86	-	68.80
Sigma	0.20	0.05	0.09	15.16	1.98	1.80	2.32	0.14	0.47	0.76	0.74	15.53	-	9.70

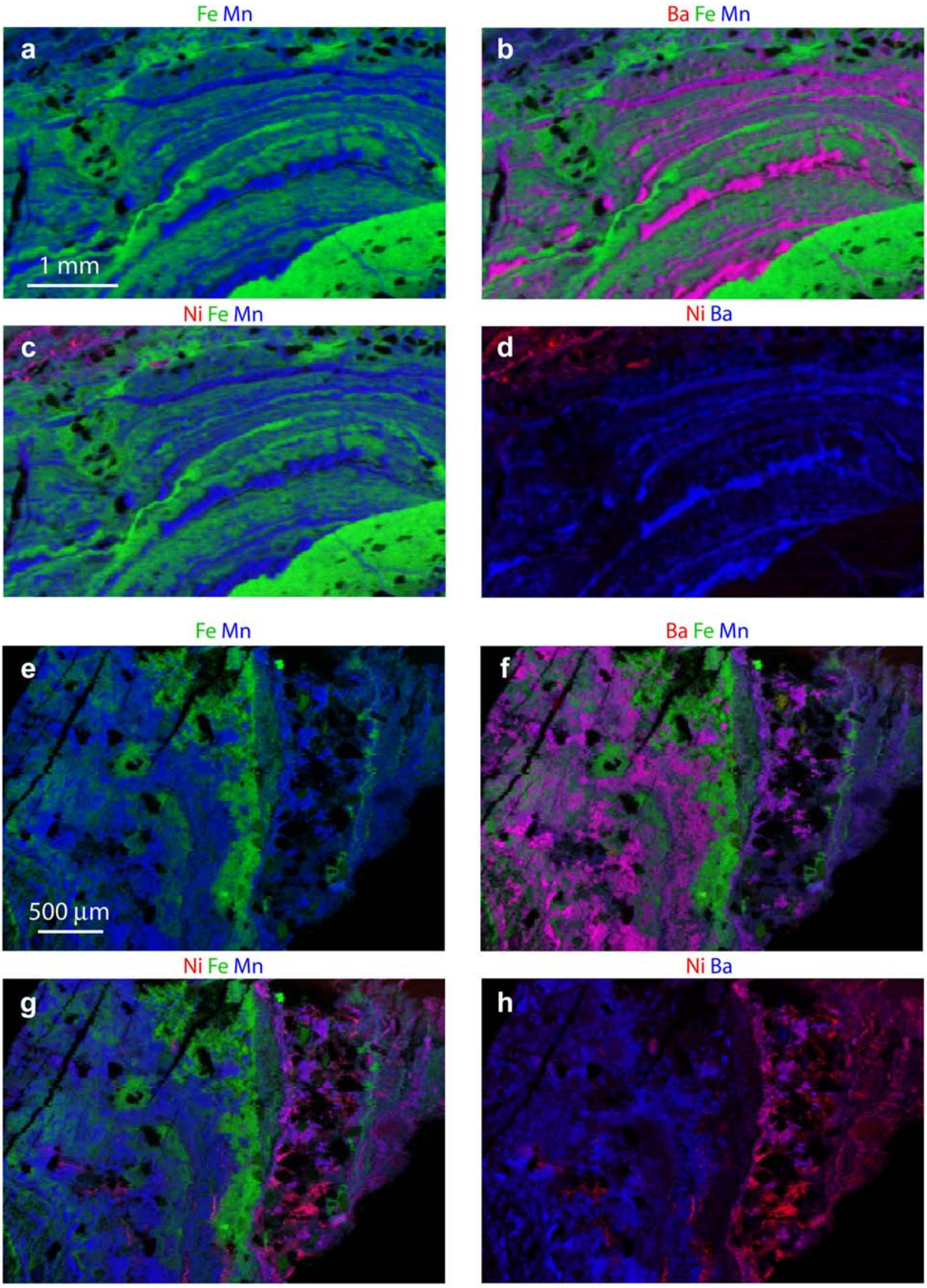

EA-4. Distribution of Mn, Fe, Ba, and Ni in two other regions of the ferromanganese nodule. The top map has a dimension of 4880 x 3000 μm^2 and a pixel resolution of 20 x 20 μm^2 (beam size 16 (H) x 7 (V) μm^2), and the bottom map has a dimension of 3400 x 2300 μm^2 and a pixel resolution of 10 x 10 μm^2 (beam size 8 (H) x 7 (V) μm^2). The color coding is the same as in Figure 1. The Mn, Fe and Ni maps were recorded at 10 keV, and the Ba map was obtained by subtracting the fluorescence intensity at 5197 eV (Ba L_3 - 50 eV) from that at 5297 eV (Ba L_3 + 50 eV) in order to get rid of the Ti(Kα) fluorescence intensity at 4966 eV. Counting time = 100 ms / pixel.

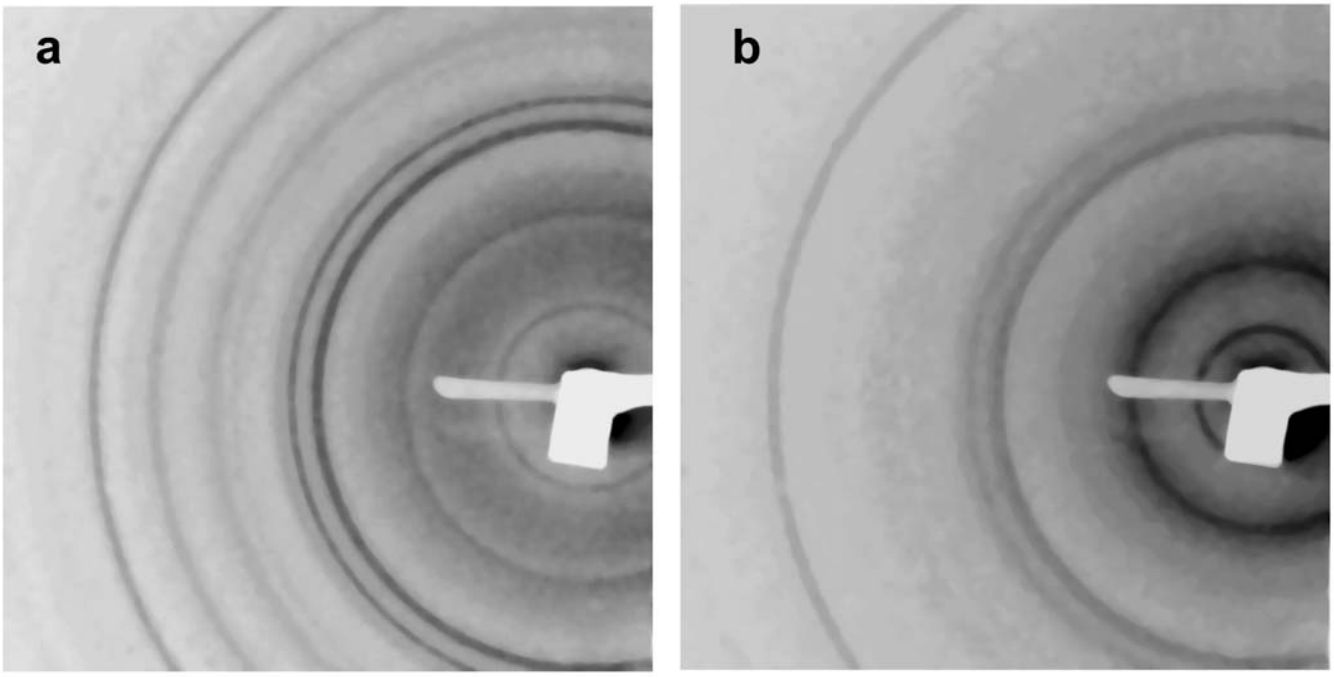

EA-5. Characteristic two-dimensional micro XRD patterns recorded in Ba-rich (a) and Ni-rich layers b).

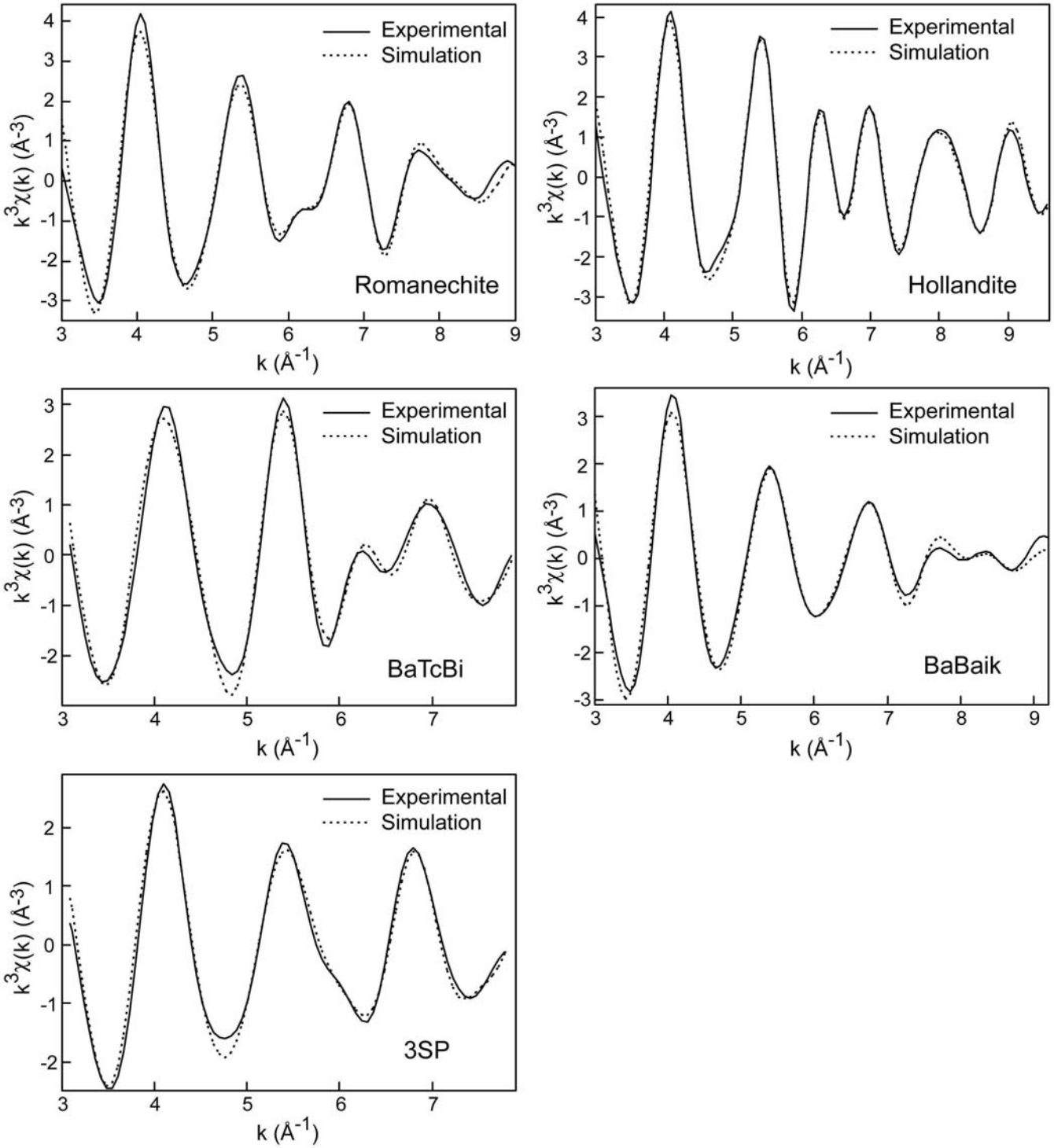

EA-6. Inverse Fourier transforms of Ba L_3-edge EXAFS spectra in the [1.5 - 5.1 Å] $R + \Delta R$ interval with spectral simulations. The data are in solid lines, and the models in dotted lines.